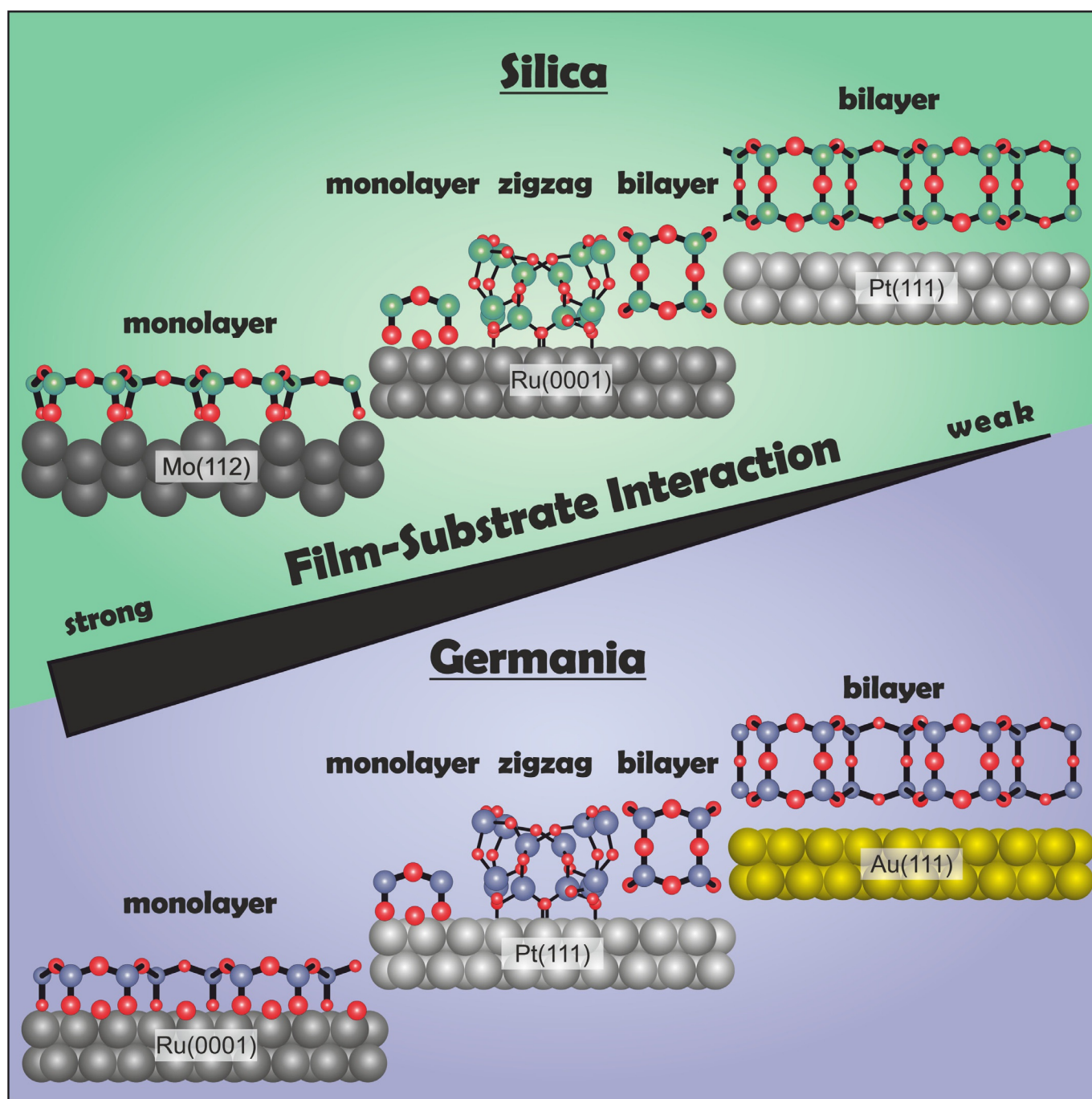


## Thin Films | Reviews Showcase |

## Growth and Atomic-Scale Characterization of Ultrathin Silica and Germania Films: The Crucial Role of the Metal Support

Adrián Leandro Lewandowski,<sup>[a]</sup> Sergio Tosoni,<sup>[b]</sup> Leonard Gura,<sup>[a]</sup> Zechao Yang,<sup>[a]</sup> Alexander Fuhrich,<sup>[a]</sup> Mauricio J. Prieto,<sup>[a]</sup> Thomas Schmidt,<sup>[a]</sup> Denis Usvyat,<sup>[c]</sup> Wolf-Dieter Schneider,<sup>[a]</sup> Markus Heyde,<sup>\*[a]</sup> Gianfranco Pacchioni,<sup>[b]</sup> and Hans-Joachim Freund<sup>[a]</sup>



**Abstract:** The present review reports on the preparation and atomic-scale characterization of the thinnest possible films of the glass-forming materials silica and germania. To this end state-of-the-art surface science techniques, in particular scanning probe microscopy, and density functional theory calculations have been employed. The investigated films range from monolayer to bilayer coverage where both, the crystalline and the amorphous films, contain characteris-

tic  $XO_4$  ( $X = Si, Ge$ ) building blocks. A side-by-side comparison of silica and germania monolayer, zigzag phase and bilayer films supported on Mo(112), Ru(0001), Pt(111), and Au(111) leads to a more general comprehension of the network structure of glass former materials. This allows us to understand the crucial role of the metal support for the pathway from crystalline to amorphous ultrathin film growth.

## Introduction

The elucidation of the atomic structure of glass is still one of the intriguing goals for material scientists. Specifically, the network structure of silica, a glass-former material, has been a topic of intense debate.<sup>[1]</sup> Recently, combining experiment and theory<sup>[2,3]</sup> a metal-supported silicon dioxide (silica) bilayer film has been characterized at the atomic scale using scanning probe microscopy (SPM). This silica bilayer film represents the first two-dimensional (2D) glass and allowed us to 'see' for the first time a vitreous structure<sup>[4]</sup> in real space.<sup>[3,5]</sup> Moreover, due to its high stability, this 2D film has been successfully transferred from one support to another without any damage.<sup>[6,7]</sup> The silica network structure has size selective adsorption properties that allowed for the realization of an atomic sieve<sup>[8-10]</sup> or even for gas storage devices.<sup>[11]</sup> Depending on the electronic structure of the atomic adsorbates, different penetration barriers have been observed. In recent experiments also chemical reactions have been characterized in a confined space environment, guided by the atomic structure of the 2D film system.<sup>[12]</sup> The importance of such a model system lies in the fact that silica is one of the most abundant materials, that it is a key component in microelectronics, and that it is a widely-used support in catalysis.

In general, oxide films present physicochemical properties characteristic for the bulk oxide material. However, the 2D confinement in very thin films and the film-support interaction may lead to unique new properties<sup>[13]</sup> rendering these materials novel and interesting for technological applications.<sup>[14,15]</sup>

The discovery of the new 2D ultrathin film material silica has initiated intense research activities to clarify under which conditions crystalline or amorphous film phases are created on various metal supports. Early investigations on ultrathin silica films on Mo(112), Ru(0001), and Pt(111) have shown that metals with high oxygen affinity favour the formation of crystalline monolayer films, whereas noble metals favour primarily vitreous silica bilayer films.<sup>[16]</sup>

To obtain a more general picture of 2D glasses, ultrathin germania films have been successfully synthesized and characterized at the atomic scale on Ru(0001),<sup>[17,18]</sup> Pt(111),<sup>[19]</sup> and Au(111).<sup>[20]</sup> These metal supports exhibit different lattice constants and significantly different chemical reactivities, so that each of them promotes the formation of different germania polymorphs. This allows us to systematize the influence of the substrate on the atomic network structure of the film. The orientation of adjacent rings, the ring-size distribution, and the ring-triplets analysis for each phase on each metal support, together with density functional theory (DFT) periodic slab calculations, suggest that the film structure is clearly affected by the film-support interactions.


The present report compares the atomic network structure of the two new 2D materials, ultrathin silica and germania films, and highlights similarities and differences between these two glass systems.<sup>[21,5,17-20]</sup> Silica and germania films with a thickness ranging from a monolayer to a bilayer, involve the three atomic-scale configurations shown schematically in Figure 1. The oxygen atoms (O, red spheres in Figure 1) which bridge the cations (Si and Ge, black spheres), link the film with the substrate or are adsorbed at the metal surface (grey spheres). The sketch does not imply that all three structures (monolayer, zigzag, bilayer) have been observed on the considered metal supports. Interestingly, those polymorphs observed in germania films, have been previously observed in silica films with, in some cases, remarkable differences.


The monolayers of both, silica and germania, are characterized by a network which is chemically bound to the metal substrate (M) through Si(Ge)-O-M bonds, forming a crystalline structure that follows strictly the registry of the support. In contrast, bilayer films interact only weakly with the metal-sup-


[a] Dr. A. L. Lewandowski, L. Gura, Dr. Z. Yang, Dr. A. Fuhrich, Dr. M. J. Prieto, Dr. T. Schmidt, Prof. W.-D. Schneider, Dr. M. Heyde, Prof. H.-J. Freund  
Fritz-Haber-Institut der Max-Planck-Gesellschaft  
Faradayweg 4–6, 14195 Berlin (Germany)  
E-mail: heyde@fhi-berlin.mpg.de

[b] Dr. S. Tosoni, Prof. G. Pacchioni  
Department of Materials Science  
Università di Milano-Bicocca  
Via R. Cozzi, 55, 20125 Milan (Italy)

[c] Dr. D. Usvyat  
Institut für Chemie  
Humboldt-Universität zu Berlin  
Brook-Taylor-Str. 2, 12489 Berlin (Germany)

 The ORCID identification number(s) for the author(s) of this article can be found under:  
<https://doi.org/10.1002/chem.202001806>.

 © 2020 The Authors. Published by Wiley-VCH GmbH. This is an open access article under the terms of Creative Commons Attribution NonCommercial-NoDerivs License, which permits use and distribution in any medium, provided the original work is properly cited, the use is non-commercial and no modifications or adaptations are made.

 Selected by the Editorial Office for our Showcase of outstanding Review-type articles <http://www.chemeurj.org/showcase>.

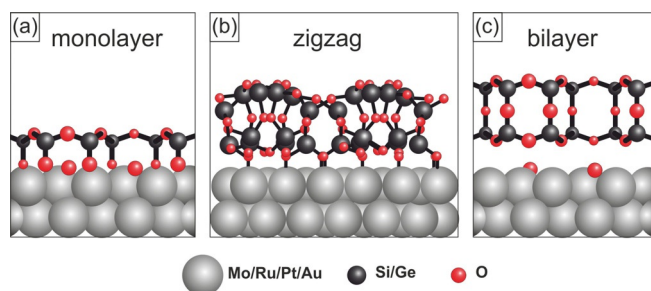


**Figure 1.** Schematic representation of the three polymorphs observed on metal-supported ultrathin films of silica and germania. The Figure has been adapted with permission from ref. [22].

port to form crystalline and/or amorphous films that ‘feel’ less the presence of the metal substrate. Finally, the zigzag phase is a crystalline metastable phase that shows an intermediate behavior between monolayer and bilayer, in terms of stoichiometry and binding to the substrate.<sup>[22]</sup>

In the following sections, the knowledge about bulk silica and germania structures, of ultrathin metal-supported silica and germania films, as well as the influence of the substrate on the film structure is presented. Special attention is given to the atomic-scale network structures of monolayer and bilayer films of germania and silica on Ru(0001), Pt(111), and on Au(111), as well as of the zigzag phase and domain boundaries. Finally, the atomic network structures of silica versus germania amorphous bilayer films on Ru(0001), Pt(111), and Au(111) will be discussed. The crucial role of the metal substrate for the atomic-scale network structure of the film will be highlighted. A few general rules concerning the properties of the metal substrate for the growth of amorphous network structures will emerge from this discussion.

## Bulk Germania and Silica Structures

Silica and germania share chemical and structural properties, thus being considered analogue systems. In particular, the building blocks in the low-pressure regime ( $XO_4$  tetrahedra,  $X = \text{Si, Ge}$ ) and in the high-pressure one ( $XO_6$  octahedra) are the same.<sup>[23]</sup> This resemblance is expected since both Si and Ge share the same group in the periodic table of the elements. Nevertheless, since Ge is placed in the period below Si, it has a larger size, thus having a germania cation–anion radius ratio close to the limiting value for the tetrahedral–octahedral structural transition, proposed by Linus Pauling.<sup>[24,25]</sup> The larger dimensions of Ge with respect to Si, enable the O to occupy more positions surrounding the cation, a fact that is reflected by certain differences in germania with respect to silica, like more distorted tetrahedra, more structural sensitivity towards pressure, much lower glass transition temperature ( $T_g$ ), larger number of 3-membered rings in the glass, among others (see Table 1).<sup>[23]</sup>

M. Micoulaut et al. have reviewed the knowledge of the crystalline and amorphous polymorphs of germania that we briefly summarize here.<sup>[23]</sup>

**Table 1.** Physical properties of bulk amorphous silica and germania as determined by X-ray diffraction (XRD), neutron diffraction (ND) and anomalous X-ray scattering (AXS). The bond lengths and angles, the glass transition temperature ( $T_g$ ) and the melting point (m.p.) are reported. The data has been extracted with permission from refs. [35–39] and the table has been published in ref. [18].

	SiO <sub>2</sub>	GeO <sub>2</sub>
M–O	0.16 nm (ND) (XRD)	0.17 nm (ND) (AXS)
O–O	0.26 nm (ND) (XRD)	0.28 nm (ND) (AXS)
M–M	0.31 nm (ND) (XRD)	0.32 nm (ND) (AXS)
O–M–O	106–114°	104–115° (ND)
M–O–M	120–180° (XRD) mean 144°	121–147° (XRD) mean 130°
$T_g$	1474 K	980 K
m.p.	1996 K	1389 K

Germania forms two crystalline polymorphs at room temperature:  $\alpha$ -quartz-like and rutile-like structures. The latter is considered as the most stable phase at room temperature and shows close resemblance with the silica rutile-like structure (stishovite) with the cations in 6-fold coordination. Conversely,  $\alpha$ -quartz-like germania is the stable phase at high temperature and presents significant differences with  $\alpha$ -quartz.<sup>[26]</sup> It consists of  $GeO_4$  tetrahedra, which are more distorted than the  $SiO_4$  unit blocks. Whereas the O–Si–O angle remains close to the ideal intratetrahedral bond angle (109.5°), O–Ge–O presents a wider distribution that ranges from 106.3 to 113.1°. The inter-tetrahedral angle has a lower mean value for germania (130°) than for silica (144°).<sup>[25]</sup> Moreover, it has been shown that by applying pressure, the  $GeO_4$  unit block gets more distorted than the analogue Si-based one.<sup>[27]</sup>

The structure of amorphous silica and germania has been mostly inferred by complementary information from neutron diffraction (ND) and X-ray diffraction (XRD), since X-ray diffraction is more sensitive to X–O, X–X bonds, and neutron diffraction to X–O and O–O bonds.<sup>[23]</sup> From these results it is concluded that the structure of both vitreous germania and silica matches the continuous random network (CRN) theory<sup>[4]</sup> in contrast to the crystallite theory.<sup>[28]</sup> The latter theory pictures the glass as an aggregate of highly dispersed crystals, whereas the CRN theory proposes the presence of corner sharing  $XO_4$  tetrahedra that are linked together randomly forming a network that lacks periodicity, extended symmetry, and long-

Markus Heyde received his PhD in Physical Chemistry from the Humboldt-Universität zu Berlin in the group of Klaus Rademann in 2001. Between 2001 and 2003, he was supported by a Feodor-Lynen research fellowship of the Alexander von Humboldt foundation and worked in the group of Miquel Salmeron at the Lawrence Berkeley National Laboratory. In 2003, he joined Hans-Joachim Freund’s department as a postdoc and later headed the Scanning Probe Microscopy as a group leader at the Fritz-Haber-Institut. In 2019 he moved within the institute to Beatriz Roldan Cuenya’s department.





range order.<sup>[29–31]</sup> However, recent analysis of the density fluctuations in vitreous silica and germania concluded that the concentration of crystalite-like areas in such glasses is too high to match a truly random network.<sup>[32]</sup>

The debate about a model that fits better the real structure of glass is still open and a theory that combines the mentioned ones, known as cybotactic theory,<sup>[33]</sup> would better explain the chemistry and devitrification behavior of glasses.<sup>[34]</sup>

Table 1 summarizes a few physical properties of vitreous silica and germania glass measured by XRD, ND and anomalous X-ray scattering (AXS).

Although the different experimental techniques agree that the silica tetrahedron is more rigid than the germania one,<sup>[38]</sup> there is no general consensus in the width distribution of the X-O-X bond angle, responsible for the medium range order of the system and hard to access. It is a widespread opinion in the literature, that the Si-O-Si angle distribution in amorphous silica<sup>[37]</sup> is much broader than in amorphous germania. However, more recent high energy XRD and nuclear magnetic resonance (NMR) experiments suggest that the distributions are actually very similar.<sup>[40,41]</sup> Apart from the angle distribution, the mean Ge-O-Ge intertetrahedral angle is smaller than the silica one (130 versus 144°).<sup>[40,42]</sup> One can note that the mean intertetrahedral angles match those of the  $\alpha$ -quartz-like structures, above described. Moreover, germania glass may present a larger number of 3-membered rings than silica.<sup>[38]</sup> Such a ring requests for a Ge-O-Ge bond angle of 130.5°.<sup>[43,44]</sup>

## Ultrathin Silica Films

The important role of silica in technology, semiconductor industry and heterogeneous catalysis<sup>[45–50]</sup> motivated us to prepare a well-defined silica model system that allows us to study its properties at the atomic scale. Using a metal single crystal as a support to grow ultrathin silica films is a successful strategy, as it provides an atomically flat, ordered and almost defect-free template on which the film can grow. Moreover, the metal provides a nearly infinite source of electrons that supply the conductivity that most surface science techniques need. Since this is only valid if the film is sufficiently thin, most of the experiments that are mentioned here are related to ultrathin silica films up to bilayer thickness.

### Historical Overview

The first experiments encompassed the successful preparation of thin, crystalline silica films supported on Mo(112).<sup>[51–53]</sup> The preparation was successfully achieved by evaporating one-half monolayer of Si at room temperature onto the metal surface with subsequent annealing steps at 800 and 1200 K together with an oxygen back pressure in the  $10^{-5}$  mbar range. Slight differences in preparation conditions were reported by the Goodman group as compared to our group. The precise atomic structure of the film was discussed controversially. There were in essence two models that agreed that the SiO<sub>4</sub> tetrahedron was the building block, the film had  $c(2 \times 2)$  periodicity and the coverage did not exceed the SiO<sub>4</sub> unit block in

thickness, but differed in the orientation and connectivity of the SiO<sub>4</sub> tetrahedra.<sup>[52,53]</sup> T. Schroeder et al., based on results obtained by X-ray photoelectron spectroscopy (XPS), ultraviolet photoelectron spectroscopy (UPS) and infrared reflection absorption spectroscopy (IRAS), proposed models inspired by silica bulk polymorphs in which the SiO<sub>4</sub> tetrahedra bind to each other and to the metal substrate.<sup>[51,52]</sup> On the other hand, M.-S. Chen et al., analysing data from high-resolution electron energy loss spectroscopy (HREELS), proposed a model described as Mo(112)- $c(2 \times 2)$ -SiO<sub>4</sub> with only one tetrahedron per unit cell with its four oxygen atoms bound directly to the metal substrate.<sup>[53]</sup>

Finally, the exact atomic structure of silica films on Mo(112) was revealed simultaneously by J. Weissenrieder et al., by combining scanning tunneling microscopy (STM), XPS, IRAS and DFT calculations,<sup>[54]</sup> and by L. Giordano et al., by comparing computed vibrational frequencies with previously reported IRAS and HREELS spectra.<sup>[55]</sup> The first 2D network of corner-sharing SiO<sub>4</sub> tetrahedra was obtained (a so-called monolayer silica film), in which three of the oxygen atoms of a unit block bridge neighboring SiO<sub>4</sub> and the fourth one bonds the substrate, in agreement with the model of T. Schroeder et al.<sup>[51,62]</sup> Figure 2 shows an atomically resolved STM image of the silica monolayer on Mo(112) and the top- and side-view DFT calculated models, reproduced from Ref. [54].

These results opened a new field of research characterized by atomically-defined silica surfaces ideal for heterogeneous catalysis experiments at the atomic level.<sup>[12,56–61]</sup>

Continuing with this approach, the first 2D zeolites were synthesized by co-deposition of Si and Al on a Mo(112)-O-precovered single crystal.<sup>[62]</sup> In these aluminosilicates, Al replaces some Si atoms hence forming an atomically flat film of corner-sharing SiO<sub>4</sub> and AlO<sub>4</sub> unit blocks. Subsequently an atomic sieve has been realized on a porous silica film on Mo(112), in which Pd atoms can penetrate through the holes in the film.<sup>[8]</sup>

Due to the fact that in the monolayer films one oxygen atom per SiO<sub>4</sub> tetrahedron is shared between the Si and metal atoms from the support, the stoichiometry of the monolayer systems is SiO<sub>2.5</sub>, different from SiO<sub>2</sub> of a fully saturated silica structure.<sup>[53–55]</sup>

In a few experimental studies also the thicker silica films have been approached. However, thicker silica films supported on molybdenum surfaces only led to ill-defined surface structures.<sup>[63,64]</sup> The growth mode of these films is conditioned by

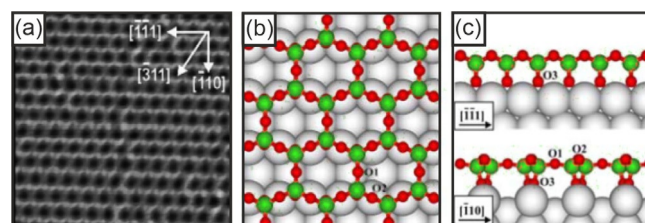


**Figure 2.** Silica monolayer film supported on Mo(112). (a) STM image, 8.0 nm $\times$ 8.0 nm,  $I_t = 0.75$  nA,  $V_s = 0.65$  V. (b) Top and (c) side view of the DFT calculated model. Si and O atoms are represented with green and red spheres, respectively. All images are adapted with permission from ref. [54].

the strong Si-O-Mo bond, as alluded to above, hence preventing a defined layer-by-layer growth.<sup>[65]</sup> As a matter of fact, the film-substrate interaction is the main impediment to grow better defined stoichiometric SiO<sub>2</sub> films. The problem was solved with the selection of the Ru(0001) crystallographic plane as an appropriate metal support which has a lower oxygen affinity.

The preparation of silica films on Ru(0001) consists of the following main steps: precover the Ru(0001) with oxygen, evaporate silicon on top, and finally anneal in oxygen at around 1200 K.<sup>[2,21,66,67]</sup> By varying slightly these parameters, different silica structures on Ru(0001) are observed. The adsorption of oxygen on Ru(0001) prior to silicon evaporation may prevent Si and Ru intermixing and provides the system with highly reactive oxygen atoms that are consumed during the evaporation process, as determined by XPS.<sup>[2,66]</sup>

Furthermore, the amount of evaporated silicon determines the coverage of the film. At low coverage, a monolayer with a similar structure to that found on Mo(112) is formed, which also shows a (2×2) periodicity in the low-energy electron diffraction (LEED) pattern and where the IRAS spectrum indicates the presence of Si-O-Ru bonds.<sup>[66,68,69]</sup> Interestingly, ultra-flat and well-defined films with SiO<sub>2</sub> stoichiometry are obtained when the coverage is doubled, that is, two layers of SiO<sub>4</sub> tetrahedra connected to each other through Si-O-Si bonds perpendicular to the metal surface (see model in Figure 1 c).<sup>[2]</sup> In this case the SiO<sub>2</sub> film is fully saturated and there are no chemical bonds linking it to the metal support. The interaction between the silica film and the Ru(0001) originates mostly from dispersion forces with an adhesion energy of magnitude 3.1 kJ mol<sup>-1</sup> Å<sup>-2</sup> calculated with DFT + D.<sup>[2]</sup> Experimentally, the absence of chemical bonds between the film and the substrate is evidenced in the now missing Si-O-Ru vibrational frequency observed on monolayer films on the same substrate only exhibiting Si-O-Si vibrations. The crystalline phase presents a unit cell twice as large as the one of Ru(0001), thus leading to a (2×2) superstructure in the LEED pattern, aligned to a high symmetry direction. The double layer now forms cages that involve twelve silicon atoms, all connected by oxygen atoms. If we only consider the Si atoms of the structure, two layers of 6-membered rings in the plane parallel to the surface are seen, separated by 4-membered rings in the perpendicular direction (see model in Figure 1 c).

Another decisive step towards the realization of a well-defined silica 2D model system was the successful preparation of a bilayer film in its amorphous phase.<sup>[21]</sup> The atomic network structure was imaged by STM and atomic force microscopy (AFM) showing no long range ordering and periodicity.<sup>[21,5]</sup> In addition, the SiO<sub>4</sub> unit blocks remain the same, however they do not follow any preferential orientation.<sup>[5]</sup> In contrast to the ordered honeycomb-like structure present in the crystalline phase, the vitreous silica bilayer exhibits a range of different ring-sizes, whereas in the perpendicular direction 4-membered rings still bridge both layers. On both crystalline and amorphous phases of the silica bilayer film a bias- and tip-dependent contrast has been observed, providing chemical sensitivity to the imaging process, which allows one to identify the sili-

con and oxygen atomic positions.<sup>[2,21]</sup> The imaging of this 2D vitreous phase permitted for the first time the direct observation of a glass at the atomic scale thus verifying directly the CRN theory proposed in 1932.<sup>[4]</sup>

The silica bilayer also allows one to computer-model amorphous systems<sup>[70–74]</sup> and compare them with experimental results in real space, since the decrease in the dimensionality from the three-dimensional (3D) bulk material<sup>[1]</sup> to 2D networks renders the calculations feasible.<sup>[75]</sup>

The silica bilayer today is in the tool box of 2D materials,<sup>[76]</sup> thanks to extensive characterization that includes studies of: work function,<sup>[77]</sup> band-gap,<sup>[78]</sup> crystalline-vitreous interface,<sup>[3]</sup> atomic<sup>[9,11]</sup> and molecular<sup>[79,11,80]</sup> sieve, confined chemistry,<sup>[59,12,60,61]</sup> bending rigidity,<sup>[81]</sup> 2D zeolites,<sup>[82–84]</sup> transferring from one substrate to another<sup>[6]</sup> and imaging in water.<sup>[85]</sup> With all this knowledge available, the silica bilayer becomes an interesting dielectric material for nanoelectronic devices.<sup>[76]</sup>

Moreover, in addition to the growth of silica bilayer films on Ru(0001), the film has been prepared on graphene,<sup>[86]</sup> Pt(111),<sup>[16]</sup> Pd(111),<sup>[87,80]</sup> Pd(100),<sup>[88,89]</sup> and Ni<sub>x</sub>Pd<sub>1-x</sub>(111).<sup>[90]</sup> The impact of the metal support on the silica film structure is the topic of the next section. Understanding the mechanisms that determine the structure of the films when prepared on different substrates is important to predict the structures of germania films on metal supports, discussed in the following sections.

### Influence of the Substrate

The structure and properties of metal-supported silica films are strongly influenced by the composition of the metal substrate.<sup>[16,90,77,91,87,90]</sup> The films adopt different atomic arrangements when prepared on different metal substrates.

Table 2 collects properties of some crystallographic planes of metals (and graphene) that have been used to support silica films. The supports are listed in decreasing order of oxygen affinity, as evidenced by their calculated heat of dissociative adsorption of O<sub>2</sub> ( $\Delta H_{ads}(O_2) = 2\Delta H_f^0(\text{metal-O}) = \Delta H_f^0(\text{O-O})$ ).<sup>[92]</sup> Regarding the substrate geometry, Ru(0001), Pt(111), Pd(111) and graphene have hexagonal symmetry, whereas Mo(112) has a 2D rectangular unit cell and Pd(001) a square one. The table also shows the kind of silica film configurations experimentally observed (tick) or not observed (cross). There is a clear tenden-

**Table 2.** Properties of some substrates used to support silica films. The following information is provided for each support: crystallographic structure; 2D lattice vectors [Å]; calculated heat of dissociative adsorption of oxygen [kJ mol<sup>-1</sup>];<sup>[92]</sup> experimental observation of silica monolayer (ML), crystalline and amorphous bilayer (BL) films.<sup>[54,66,2,21,88,89,87,80,16,86]</sup>

Support	Cryst. struct.	2D lattice vectors [Å]	$\Delta H_{ads}(O_2)$ [kJ mol <sup>-1</sup> ]	ML	Cryst. BL	Amorph. BL
Mo(112)	bcc	2.72 × 4.45	-544	✓	×	×
Ru(0001)	hcp	2.70 × 2.70	-220	✓	✓	✓
Pd(100)	fcc	2.77 × 2.77	-170	×	✓	✓
Pd(111)	fcc	2.75 × 2.75	-170	×	✓	✓
Pt(111)	fcc	2.77 × 2.77	-133	×	×	✓
graphene		2.46 × 2.46		×	×	✓

cy to form bilayer films at less negative values of  $\Delta H_{ads}(O_2)$ . In addition, the crystalline bilayer films on Pd(111) and Pd(001) are non-commensurate, whereas the one on Ru(0001) forms a  $(2 \times 2)$  superstructure.

The impact of the metal substrate on the atomic structure of silica films is caused by the interplay between three main components: (1) film–substrate interaction, (2) lattice mismatch, (3) substrate geometry.<sup>[87]</sup>

X. Yu et al. suggest that the  $\Delta H_{ads}(O_2)$  of the metal substrate determines the structure of the silica film, whereas the lattice mismatch is not a critical element.<sup>[16]</sup> The trend shows that supports with high oxygen affinity, such as Mo, form chemically bonded monolayer films; metals with less oxygen affinity, like Pd and Pt, interact more weakly with the film and permit the formation of non-commensurate crystalline structures, as well as decoupled amorphous bilayer films; and intermediate metal supports, such as Ru, permit to adopt both structural polymorphs.

On the other hand, J.-H. Jhang et al. put the emphasis on the lattice mismatch to explain the different configurations adopted by the bilayer films.<sup>[87]</sup> The trend observed on silica bilayer films supported on Ru(0001), Pd(111) and Pt(111) (surface lattice constants: 2.70, 2.75, 2.77 Å, respectively) supports this argument: Bilayer films on those substrates exhibit lattice mismatches of 2.2, 3.8 and 4.6%, respectively, and thus the first one leads to the formation of a commensurate crystalline film, the second to a non-commensurate crystalline film and on the third one to only amorphous films. In support of this argument, A. Malashevich et al. have shown theoretically that tensile strain favors the formation of larger rings.<sup>[91]</sup> Experimentally, a zero-strain film has been grown on a  $Ni_{0.48}Pd_{0.52}(111)$  surface, resulting in a crystalline phase, in agreement with this argument.<sup>[90]</sup> One must clarify, that when the film–interaction is too strong, this argument is no longer valid, because then chemical interactions govern the structure, as it has been shown by doping the silica film with Al.<sup>[87]</sup>

## Monolayer Films: A Comparison

In Figure 3, the germania monolayer film supported on Ru(0001) and the germania monolayer phase that predominates at higher oxidation temperatures on Pt(111)<sup>[93]</sup> are compared to each other and to the silica monolayer film on Ru(0001). The analysis is carried out by means of STM images, and side- and top-views of the DFT calculated models of the three different monolayer films. First, the silica and the germania monolayer films on Ru(0001) (first and second columns in the Figure, respectively) exhibit a similar network of  $XO_4$  ( $X = Si$  or  $Ge$ ) tetrahedra which are chemically bound to the substrate through  $XO-Ru$  bonds and form a hexagonal  $(2 \times 2)$  superstructure (see orange unit cells in Figures 3a and b).<sup>[66,17]</sup> They differ, however, in the intertetrahedral bonding angles. Whereas the oxygen bridge in the  $Si-O-Si$  bond is straight when looked from the top (Figure 3d), the  $Ge-O-Ge$  bond is longer than  $Si-O-Si$  and forms an angle of  $150^\circ$  (Figure 3e). Moreover, they both contain an oxygen atom adsorbed in a hcp hollow site of the Ru(0001) in the center of each 6-membered ring, as

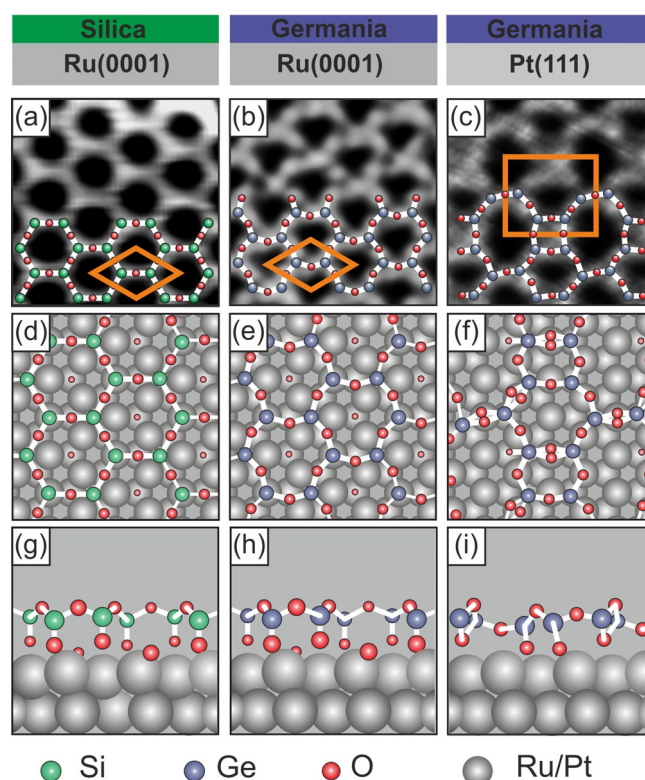


**Figure 3.** Comparison of different silica and germania monolayer films supported on Ru(0001) and Pt(111). All STM images have a size of  $2.2 \text{ nm} \times 2.2 \text{ nm}$  (first row). The top-view of the DFT calculated models have a size of  $1.5 \text{ nm} \times 1.5 \text{ nm}$  (second row), and the side-view models are shown in the third row. (a)  $I_T = 0.01 \text{ nA}$ ,  $V_S = 1.0 \text{ V}$ . (b)  $I_T = 0.2 \text{ nA}$ ,  $V_S = 0.6 \text{ V}$ . (c)  $I_T = 0.6 \text{ nA}$ ,  $V_S = 1.5 \text{ V}$ . (d)  $I_T = 0.8 \text{ nA}$ ,  $V_S = 0.8 \text{ V}$ . The Figure has been reproduced with permission from ref. [93].

determined by  $I/V$ -LEED for germania<sup>[17]</sup> and by STM for silica.<sup>[69]</sup>

Why does germania form monolayer films on Pt(111) and silica does not? On the one hand, the larger lattice constant of Pt(111) with respect to Ru(0001) implies a considerable stretching of the silica and, to a lesser extent, of the germania monolayer film to match a  $(2 \times 2)$  superstructure. In the case of germania, the tensile stress is overcome in two different ways: At low annealing temperatures germania forms a network of 6-membered rings which are rotated by  $30^\circ$  with respect to a highly symmetric direction of the Pt(111) surface.<sup>[93]</sup> Secondly, the most stable monolayer phase of germania on Pt(111) forms different ring-sizes (other than the prevailing 6-membered rings) and has a rectangular unit cell (third column in Figure 3).<sup>[19]</sup> In both cases (hexagonal and rectangular monolayer phases) the films exist due to the presence of highly distorted germania tetrahedral unit blocks. Furthermore, in the case of the rectangular configuration some Ge atoms are coordinated with five O atoms, as pictured in the DFT calculated model in Figures 3f and i. These observations are in line with the more distorted tetrahedra that bulk germania presents in comparison to bulk silica.

Moreover, the thermodynamic competition between the formation of a monolayer and a bilayer film has to be taken into



account. If the formation of a bilayer film implies an energetic benefit for the system, the tetrahedra that form the monolayer may decouple from the substrate, flip around, bind to another layer of  $\text{XO}_4$  building blocks and form a self-saturated bilayer film. This can only happen if the  $\text{XO}-\text{M}$  chemical bonds are weak enough to break and to form new  $\text{X}-\text{O}-\text{X}$  bonds. At this point, the stability of the free-standing silica and germania bilayer films and the nature of the metal substrates play a key role. Given the weakness of the  $\text{Si}-\text{O}-\text{Pt}$  bond<sup>[16,94]</sup> and the larger stability of the silica free standing bilayer film in comparison to the germania one,<sup>[91,18,19]</sup> the behavior of silica on Pt(111) seems understandable.

## Zigzag Phase: A Comparison

Recently, a silica polymorph was discovered, which is characterized by a zigzag-line contrast observed with the STM. Experimental and theoretical work resulted in a complex atomic model that combines features of the silica monolayer and bilayer networks, and some unique characteristics, like the presence of 3-membered rings.<sup>[22]</sup> A STM image and the top- and side-view of the DFT calculated model are reproduced in Figures 4a, d and f, respectively. The importance of this polymorph lies in the fact that after subsequent annealing at higher temperature, it converts completely into a silica bilayer film. Consequently, this silica polymorph represents a metastable phase, which may play an important role in the glass formation process.<sup>[22]</sup>

Metastable phases with such structural motives should be present in other glass forming materials. In fact, an analogue phase of the zigzag silica film has also been observed in germania films when being prepared at low annealing temperatures (770 K).

Figure 4b exhibits an STM image of the zigzag phase that silica forms on Pt(111). Its contrast looks very similar to the one on Ru(0001). Also the size of the unit cell (orange rectangle in the Figure) on Pt(111) corresponds to the one on Ru(0001). At the bottom part of the image the extra features can be associated with 6-membered rings embedded in the zigzag network. Similar motifs have been observed on films supported on Ru(0001).<sup>[22]</sup>

A high-resolution STM image of germania supported on Pt(111) forming a zigzag-line phase is shown in Figure 4c, together with the top- and side-view of the DFT calculated model (Figures 4e and g, respectively). The DFT model for germania obeys the same connectivity rules as those for silica, that is, non-planar 8-membered rings from the top-view, 3- and 4-membered rings from the side-view and the stoichiometry is  $\text{XO}_{2.17}$ .<sup>[22]</sup> For clarity, one non-planar 8-membered ring is marked in the STM image and in the DFT model.

The unit cell of the germania zigzag phase is also rectangular with a size of  $9.6 \text{ \AA} \times 8.3 \text{ \AA}$ , identical to the rectangular germania monolayer phase on Pt(111). This periodicity and commensurability with the metal substrate imply a significant difference to the silica zigzag-phases supported on Ru(0001), which is incommensurate and its unit cell has a size of  $9.4 \text{ \AA} \times 7.6 \text{ \AA}$ .<sup>[22]</sup> The same size of the unit cell is measured with

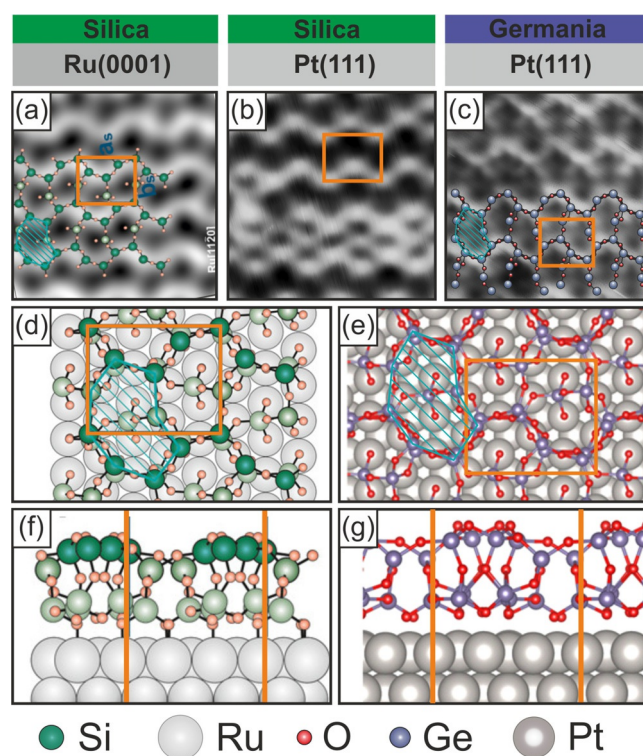


**Figure 4.** Comparison of germania and silica zigzag phases on Ru(0001) and Pt(111). The first row compares STM images of the systems illustrated on the top of the Figure. The STM images have a size of  $3.3 \text{ nm} \times 3.3 \text{ nm}$ . (a)  $I_T = 0.02 \text{ nA}$ ,  $V_S = 0.7 \text{ V}$ . (b)  $I_T = 0.8 \text{ nA}$ ,  $V_S = 0.9 \text{ V}$ . (c)  $I_T = 0.6 \text{ nA}$ ,  $V_S = 0.3 \text{ V}$ . DFT calculated models for the silica zigzag phase on Ru(0001) are shown in (d) and (f), and for the germania one on Pt(111) in (e) and (g). The unit cells are marked in orange and 8-membered rings are shaded with blue lines. Figures (a), (d) and (f) have been taken with permission from ref. [22].

the STM for the silica zigzag-phase on Pt(111). Atomic coordinates derived from the DFT calculated models are superimposed onto the corresponding STM images in Figures 4a and c. The zigzag contrast is nicely reproduced by a wavy chain of  $\text{Si}(\text{Ge})-\text{O}$  bonds. Between the zigzag-lines, less intense protrusions, corresponding to atomic positions located below the top-most layer of atoms, are also observed and superimposed with smaller spheres. Interestingly, a few atoms, which were theoretically predicted but not experimentally observed in the silica zigzag phase,<sup>[22]</sup> are now visualized in the germania one.

## Line and Other Defect Structures: A Comparison

A material with a single homogeneous crystalline phase is an idealization. There is no material that is formed exclusively by an unequivocal continuous repetition of its unit cell. The structure of bulk materials and their surfaces contain defects of many types, such as voids, dislocations, interstitials, impurities, vacancies, grain boundaries, and others, depending on the nature and synthesis of the material. Interestingly, many properties of solids are more dependent on the presence, amount and type of defects than on the structure itself.<sup>[95]</sup> As a matter of fact, defect structures in materials are often desired, since

they are responsible for controlling mechanical,<sup>[96–97]</sup> optical,<sup>[99]</sup> electronic,<sup>[100,101]</sup> and chemical properties,<sup>[102–107]</sup> which often lead to devices with practical functionalities. The influence of the defects on the material properties is enhanced by decreasing the dimensionality of materials, for instance, on surfaces. In particular, the presence of defects on oxide surfaces plays a pivotal role in heterogeneous catalysis, since they determine corrosion resistance, molecular adsorption, and reactivity.<sup>[108]</sup>

The properties of 2D materials are therefore significantly affected by the presence of defects. An exemplary case is graphene.<sup>[113,114]</sup> It has been found that the mechanical properties of graphene are not only influenced by the density of defects, but also by the atomic local arrangement of them.<sup>[98,115]</sup> Thus, it is of fundamental and of technological interest to investigate in detail the atomic configuration of defects and grain boundaries to understand the effect on the material properties. As an example, whereas the main phase of graphene consists of hexagons of six carbon atoms each, grain boundaries are formed mostly by pentagon–heptagon pairs.<sup>[114]</sup> More details about the defects of graphene layers can be found in the Review of F. Banhart, et al.<sup>[116]</sup>

Table 3 shows a summary of the ring-size configuration of different defects and domain boundary structures observed in graphene and in ultrathin films of germania and silica. The main source of defect formation in the ultrathin films lies in the structural mismatch, e.g., different lattice constants, of the supporting substrate and the film.<sup>[111]</sup> In the case of graphene, note that Table 3 only shows such defects that have been experimentally identified to date, excluding the vast list of predicted ones.<sup>[117,118]</sup>

The majority of defects in graphene are observed with transmission electron microscopy (TEM). They correspond mostly to point defects, in contrast to the silica and germania defects which form domain boundary structures (Table 3). An exception is the Stone–Wales defect (in which four adjacent 6-membered rings are changed into two 5-membered rings and two 7-membered rings<sup>[119]</sup>) that is present in graphene and in silica bilayer films on Ru(0001). This may suggest that such defects are only formed in well-decoupled systems. Furthermore, the 558 is the most common antiphase boundary structure, observed in graphene, in the silica bilayer on Ru(0001) and in the germania monolayer on Ru(0001). The germania monolayer film on Ru(0001) is the system with the largest amount of different defect structures, despite its chemical bond to the metal-support. The flexible GeO<sub>4</sub> building blocks, which lead to a wide set of ring combinations may be the origin of these defect structures.

## Bilayer Films: A Comparison

For free-standing germania and silica bilayer films the 6-membered ring configuration is predicted to be the most stable polymorph by means of DFT.<sup>[91,18,19]</sup> The hexagonal germania bilayer film presents a more distorted structure, characterized by:<sup>[91,18,19]</sup> (1) Ge–O–Ge bond angles in the direction perpendicular to the surface which are smaller than the 180° Si–O–Si bond angles in the silica bilayer film; (2) a reduced symmetry,

**Table 3.** Line and other common defect structures in graphene, and ultrathin films of silica and germania.

System	Types	Method	Ref.
Graphene	Stone–Wales defect	TEM	[109]
	59 point defect	TEM	[110]
	585 point defect	TEM	[110]
	555777 point defect	TEM	[110]
	555567777 point defect	TEM	[110]
ML SiO <sub>2</sub> /Ru(0001)	558 domain boundary	STM	[111]
	5577 domain boundary	STM	[69]
	57 triangular loop defect encompassing a 6 MR	STM	[68]
BL SiO <sub>2</sub> /Ru(0001)	457 rectangular loop defect encompassing an 8 MR	STM	[68]
	558 antiphase domain boundary	AFM/STM	[112]
	57 rotational domain	AFM/STM	[9]
	48 domain boundary	AFM/STM	[9]
ML GeO <sub>2</sub> /Ru(0001)	Stone–Wales defect	AFM/STM	[9]
	57 closed-loop defects	AFM/STM	[9]
	48 antiphase domain boundary	STM	[17]
	57756 antiphase domain boundary	STM	[17]
	5678 complex boundary	STM	[18]
	58 triangular loop defect encompassing a 6 MR	STM	[18]
ML GeO <sub>2</sub> /Pt(111) (Hexagonal)	45678 loop defect encompassing three 6 MR	STM	[18]
	558 antiphase domain boundary	STM	[18]
ML GeO <sub>2</sub> /Pt(111) (Rectangular)	elongated 8 MRs	STM	[93]
BL GeO <sub>2</sub> /Pt(111)	antiphase domain boundary	STM	[93]
	6 MR antiphase domain boundary	STM	[19]

$D_{3r}$  in comparison to the symmetry of the silica bilayer film,  $D_{6hr}$  due to the rotation of the top and bottom tetrahedra building blocks that removes the mirror plane between the upper and the lower layer breaking the  $C_6$  rotational axis; (3) less stable rings other than 6-membered rings compared to those of the silica bilayer film; (4) a considerably lower stability than the silica bilayer film.

After adsorption of the film on a metal substrate, an important parameter to evaluate the coupling between the film and the substrate is the adhesion energy ( $E_{ad}$ ). It refers to the relaxation of the system when covering a bare substrate with a film, and it is defined as follows:<sup>[18]</sup> [Eq. (1)]

$$E_{ad} = [E(XO_2/M) - E(M) - E(XO_2)]/S \quad (1)$$

Where  $E$  is the total electronic energy (per supercell) of the  $XO_2/M$  supported film (including the contribution of the long-range dispersion),  $M$  is the energy of the support, the last term is the energy of the free-standing film; and  $S$  is the supercell area. Note that negative adhesion energy indicates bonding of the film to the substrate. The more negative the adhesion energy is, the stronger is the film–substrate bonding, i.e., the film–substrate interaction increases with increasing negative



adsorption energy. In addition, there are other important parameters to probe the film–substrate interaction:<sup>[18]</sup> the film–substrate distance ( $d$ ), defined as the average distances in the  $z$ -direction between the uppermost metal layer and the lowest oxygen layer of the film; and  $Q$ , the charge transfer from the substrate to the film.

Table 4 shows the DFT calculated  $E_{\text{ad}}$ ,  $d$  and  $Q$  for the hexagonal and the 558 configuration for the germania bilayer films supported on Ru(0001), Pt(111) and Au(111); and for the silica bilayer films on Ru(0001) and Pt(111).

Due to the difficulty to calculate the Au(111) so called heringbone reconstruction, two different domains (fcc and hcp) have been modeled as discussed in refs. [120,20]. All the adhesion parameters show a moderate dependence on the Au(111) domain. Moreover, the germania bilayer film supported on Au(111) is characterized by a weak film–substrate interaction, manifested in a low  $E_{\text{ad}}$ , a large  $d$  and low  $Q$ , as shown in Table 4.

Conversely, the  $\text{GeO}_2/\text{Ru}(0001)$  system has a four times increased  $E_{\text{ad}}$  compared to the one of  $\text{GeO}_2/\text{Au}(111)$ , a 0.08 nm shorter  $d$  and a significant larger  $Q$  value (see Table 4). The latter is related to charge transfer from the Ru(0001) substrate to the germania film that gives rise to Ge and O states right above and below the Fermi level in the calculated density of states.<sup>[18]</sup> These adhesion parameters point towards the formation of chemical bonds between the film and the substrate, which are responsible for the highly stable monolayer films and buckled bilayer structure. A similar behavior has been observed for silica films on Mo(112), as discussed in section 4.

On the other hand, the germania films supported on Pt(111) bear a close resemblance to the silica films on Ru(0001). Firstly, in both cases the interaction between the film and the substrate is such that it permits the presence of different polymorphs: monolayer film, zigzag phase and bilayer film. Secondly, within the bilayer phases, both systems present a crystalline and an amorphous configuration. This new 2D germani-

um dioxide film consists of interconnected germania tetrahedral units forming a bilayer structure, weakly coupled to the supporting Pt(111) metal–substrate.<sup>[19]</sup> Figure 5 compares side-by-side the hexagonal crystalline phase of the silica bilayer film on Ru(0001) (left-hand column) and the 558 phase of the germania bilayer film on Pt(111) (right-hand column). In agreement with the ring-sizes observed with the STM (Figures 5a and b), DFT calculations predict a stable structure of 6-membered rings for silica films (Figures 5c and e) and 558-membered rings for germania films (Figures 5d and f). Whereas the crystalline silica bilayer film on Ru(0001) has a hexagonal symmetry, the germania film on Pt(111) forms an oblique unit cell constituted by two 5-membered rings and one elongated 8-membered ring (the unit cells are marked in black in the Figure). By looking at the side-views of the DFT models (Figures 5e and f), one can notice the larger degree of distortion of the germania film. The adhesion properties for both systems,  $\text{SiO}_2/\text{Ru}(0001)$  (hex) and  $\text{GeO}_2/\text{Pt}(111)$  (558), are com-

**Table 4.** Comparison of adhesion properties of metal-supported germania and silica bilayer films calculated at the PBE/D2' level: strain [%], adhesion energy ( $E_{\text{ad}}$ , eV/nm<sup>2</sup>), interfacial distance ( $d$ , nm) and charge transferred to the film normalized per surface unit ( $Q$ ,  $|e|/\text{nm}^2$ ). The coincidence of the film and the substrate cell is indicated in the footnotes. The table has been reproduced from ref. [20].

Oxide	Support	Phase	Strain [%]	$E_{\text{ad}}$ [eV/nm <sup>2</sup> ]	$d$ [nm]	$Q$ [ $ e /\text{nm}^2$ ]	Ref.
GeO <sub>2</sub>	Ru(0001)	Hex <sup>[a]</sup>	+0.24	−6.78	0.217	0.60	[18]
		558 <sup>[b]</sup>	+1.7, +3.0	−7.46	0.219	2.10	[19]
	Pt(111)	hex <sup>[a]</sup>	+1.63	−2.20	0.288	0.34	[19]
		558 <sup>[b]</sup>	+0.12, −1.23	−2.71	0.258	0.66	[19]
Au(111)	hex(fcc) <sup>[c]</sup>	−1.26	−1.54	0.301	0.35	[20]	
	hex(hcp) <sup>[d]</sup>	+0.77	−1.75	0.305	0.39	[20]	
SiO <sub>2</sub>	Ru(0001)	hex <sup>[a]</sup>	+2.76	−1.76	0.265	0.09	[18]
		558 <sup>[b]</sup>	+5.76, 4.57	−1.13	0.263	0.79	[19]
	Pt(111)	hex <sup>[a]</sup>	+4.56	−1.34	0.319	0.04	[19]
		558 <sup>[b]</sup>	+7.52, +6.34	−0.65	0.285	0.11	[19]

[a]  $(1 \times 1)/(2 \times 2)$ , [b]  $(2 \times 3)/(\sqrt{67} \times \sqrt{147})R12^\circ$ , [c]  $(3 \times 3)/(\sqrt{31} \times \sqrt{31})R9^\circ$ , [d]  $(3 \times 3)/(\sqrt{61} \times \sqrt{61})R26^\circ$ .

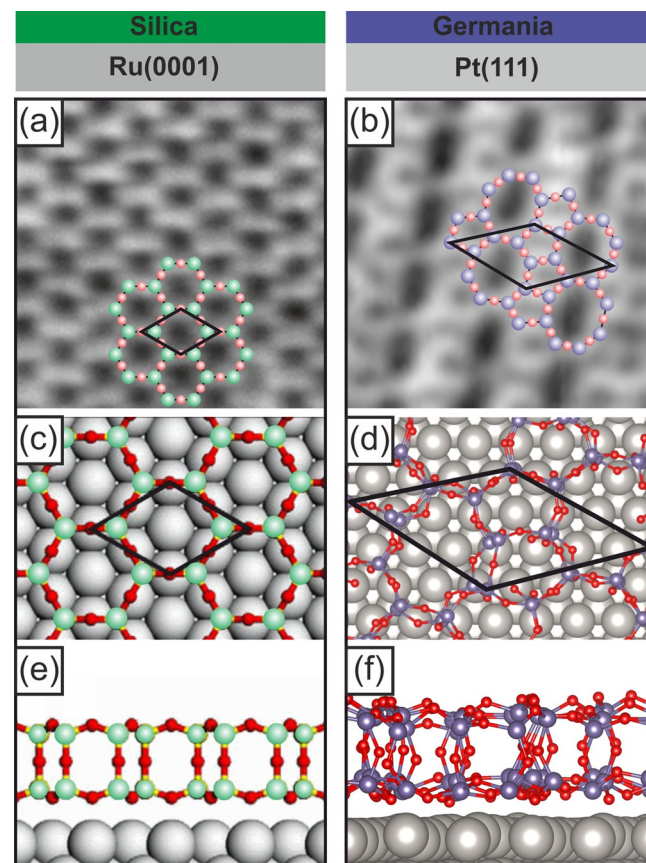


**Figure 5.** Comparison of silica (left-hand column) and germania (right-hand column) crystalline bilayer films supported on Ru(0001) and Pt(111), respectively. Figures (a) and (b) compare STM images of dimensions 3.8 nm × 3.8 nm. The crystalline bilayer phase of silica consists of 6-membered rings, whereas the germania one on Pt(111) forms an arrangement of 5- and 8-membered rings. Figures (c) and (e) exhibits the top- and side-view, respectively, of the most stable DFT calculated model for the silica bilayer supported on Ru(0001), reproduced from Ref. [2]. Figures (d) and (f) shows the DFT model of the 558 germania bilayer film on Pt(111), reproduced from ref. [2]. Si atoms are represented with green, Ge with blue and O with red spheres. (a)  $I_T = 0.1$  nA,  $V_S = 2.0$  V, reproduced from ref. [19]. (b)  $I_T = 0.4$  nA,  $V_S = 0.3$  V, reproduced with permission from ref. [19].

pared in Table 4. The distance between film and interface is similar, however, the  $E_{ad}$  is around 1 eV lower for the germania film and  $Q$  is also more significant (0.66 versus 0.09  $|e|/\text{nm}^2$ ). These parameters indicate that the germania bilayer film interacts stronger with the metal support than the silica film does, a fact that is evidenced in the „promoted“ 558 germania crystalline structure.<sup>[19]</sup> As mentioned above, in the absence of the substrate the hexagonal six-membered ring phase is favored.

Interestingly, the degree of order in the germania bilayer film supported on Pt(111) may be tuned by varying the preparation conditions. Crystalline, intermediate ordered and purely amorphous film structures are resolved by analyzing STM images.<sup>[19]</sup> A side-by-side comparison between the amorphous bilayer phases of germania on Pt(111) and of silica on Ru(0001) is the topic of the next section.

When the film–substrate interaction diminishes, purely amorphous germania bilayer films are expected to grow. A pertinent example is the growth of an amorphous germania bilayer film on a herringbone reconstructed Au(111) surface,<sup>[20]</sup> and references therein. The presence of the film affects the native configuration of the fcc and hcp stacking of the reconstructed Au(111) top layer atoms,<sup>[121]</sup> as observed with STM (see Figure 6d). The fcc and hcp reconstruction walls partly avoid the film islands, and partly penetrate underneath film patches (not shown here, see ref. [20]) This behavior indicates a weaker film–substrate interaction than the one reported for other oxide films on reconstructed Au(111), where the herringbone reconstruction is lifted. Moreover, this system highlights the impact of the metal–support on the structure of ultrathin films of germania and silica: With decreasing film–substrate interaction the propensity to form the amorphous phase of these glass forming materials increases. DFT calculations confirm and rationalize the experimental observations.<sup>[20]</sup>

Different ring-sizes have been identified in the germania bilayer film on Au(111), as shown in Figure 6f. Although on the basis of the experimental data presented in this Figure it is difficult to quantify a statistically significant ring-size distribution, a prevalence of 6-membered rings is observed. Moreover, the 6-membered rings tend to be adjacent, making the (6,6,6) triplet combination a preferred one. This result is different from the triplet analysis performed on amorphous germania bilayer films on Pt(111), where the (6,6,6) triplet combination is very rare.<sup>[19]</sup> We deduce that the ring-size distribution of the germania bilayer film supported on Pt(111) is influenced by the metal–support and, therefore, the 558 crystalline configuration, prevails.

The germania bilayer film on Au(111) shows a small adhesion energy, a large interfacial distance and low charge transfer, in comparison to other germania bilayer films (see Table 4). A similar interfacial distance (0.312 nm) has been calculated for a NaCl bilayer film supported on Au(111), an ideal physisorbed film.<sup>[122,123,120,20]</sup> Moreover, similar adhesion properties are observed for SiO<sub>2</sub>/Pt(111), in agreement with the structural similarities. The similarity is mainly related to the weak influence of the support on the film structure, which is manifested by the fact that neither monolayer films, nor crystalline bilayer phases have been observed in these systems.

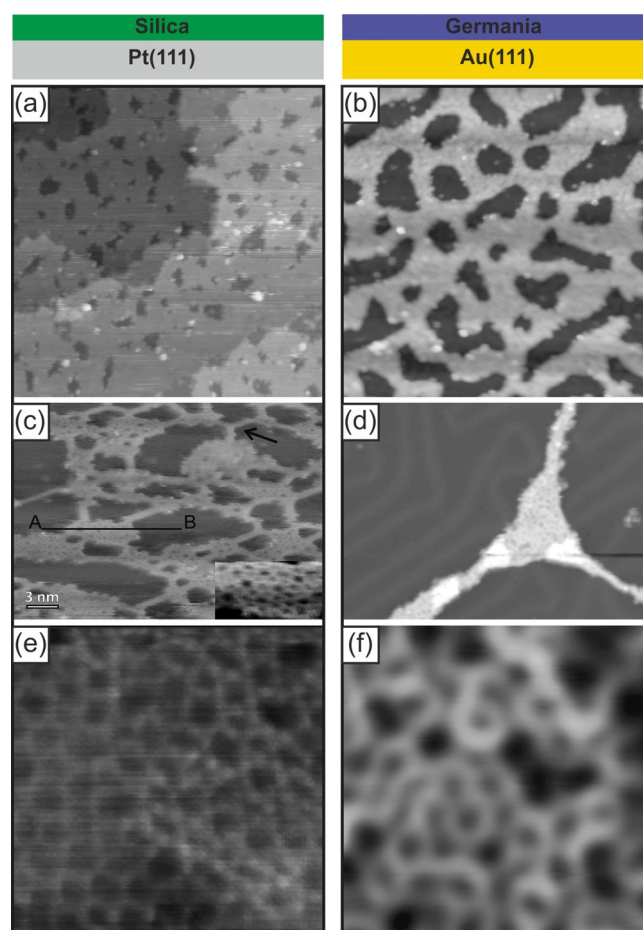


**Figure 6.** Comparison of silica (left-hand column) and germania (right-hand column) bilayer films supported on Pt(111) and Au(111), respectively. The first row compares 100 nm x 100 nm STM images of highly covered films, the second row shows 30 nm x 20 nm STM images of low covered films, and in the third row 5 nm x 5 nm STM images of the amorphous structure are shown. (a)  $I_T = 0.1$  nA,  $V_S = 4.4$  V. (b)  $I_T = 0.3$  nA,  $V_S = 0.2$  V. (c)  $I_T = 0.06$  nA,  $V_S = 0.8$  V. (d)  $I_T = 0.6$  nA,  $V_S = 2.3$  V. (e)  $I_T = 0.13$  nA,  $V_S = 1.3$  V. (f)  $I_T = 0.2$  nA,  $V_S = 0.15$  V. Figures (a), (c) and (e) are reproduced with permission from ref. [16] and Figures (d) and (f) from ref. [20].

Furthermore, the germania bilayer on Au(111) behaves like the calculated free-standing bilayer film, as the 6-membered ring is the preferred ring-size. Figure 6 compares side-by-side silica bilayer films supported on Pt(111) (left-hand column) and germania bilayer films on Au(111) (right-hand column). The Figure shows large-scale STM images of two bilayer films at high coverage (first row) and at low coverage (second row). In the high coverage regime both bilayer films grow atomically flat and form holes that expose the metal–support (Figures 6a and b). Interestingly, by preparing films with less Si(Ge) the bilayer configuration persists and forms islands that are bridged by narrow stripes (Figures 6c and d).<sup>[16,20]</sup> It is important to remark that regardless of the coverage and the preparation conditions, the silica and germania bilayer films on Pt(111) and Au(111), respectively, are always amorphous, as shown in Figures 6e and f.

An interesting classification of the structural behaviour of the films emerges when the three metal-supported germania

and silica bilayer systems are compared with respect to the strength of the film–substrate interaction reflected in their corresponding adhesion energies (see Table 4). Figure 7 depicts schematically the decreasing adhesion energy (from top to bottom) for silica and for germania films on the different metal supports. This comparison reveals that the following atomic network structures resemble closely to each other: SiO<sub>2</sub>/Mo(112) to GeO<sub>2</sub>/Ru(0001), SiO<sub>2</sub>/Ru(0001) to GeO<sub>2</sub>/Pt(111), and SiO<sub>2</sub>/Pt(111) to GeO<sub>2</sub>/Au(111).

There is, of course, an important process that we have not addressed so far, that is, the transformation and its atomistic description, for example, by STM measurements, between the crystalline and the vitreous phases. While we are working on setting up instrumentation,<sup>[124]</sup> that may allow us in the future to contribute to an atomistic understanding of the process, we are in the position to report on a recent investigation of the transformation using a temperature dependent low-energy electron microscopy/diffraction (LEEM/LEED) study. Figure 8a schematically shows the crystalline and vitreous structures along with their respective LEED pattern: well resolved spots for the crystalline and typical ring structures for the vitreous phase (the outermost spots are due to the Ru(0001) substrate). LEEM I–V measurements (not shown, see ref. [67]) show that both bilayer polymorphs exhibit different electron reflectivity at specific energies. Based on these results, the crystalline to vitreous transformation was followed in real-time in LEED at a predefined electron energy (42 eV) whereas rapidly increasing the sample temperature to the final desired value at which the transformation occurred. By determining the time dependence of the (00)-spot intensity at different temperatures it was possible to assess the energetic aspects of the phase transformation. Details of the analysis performed can be found in reference [125], as well as a detailed discussion of the proposed mechanism.

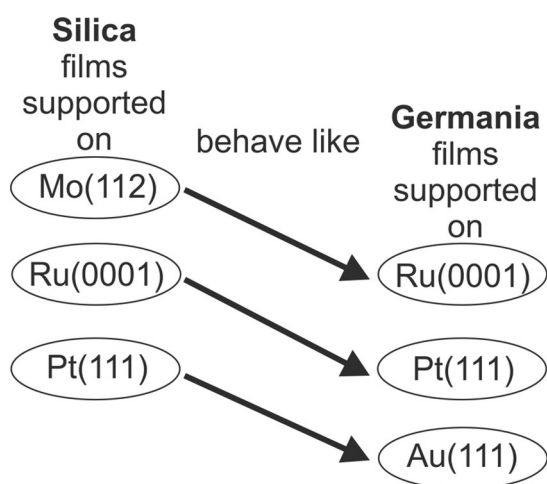


**Figure 7.** Correlation between the structural behaviour of ultrathin films of silica and germania supported on different metal substrates. The strength of the interaction (reflected in the calculated adhesion energies presented in Table 4) between the film and the substrate controls the resulting structure. The interaction decreases in each column from the top to the bottom. The weakest film–substrate interaction is found for germania on Au(111) promoting an amorphous film structure.

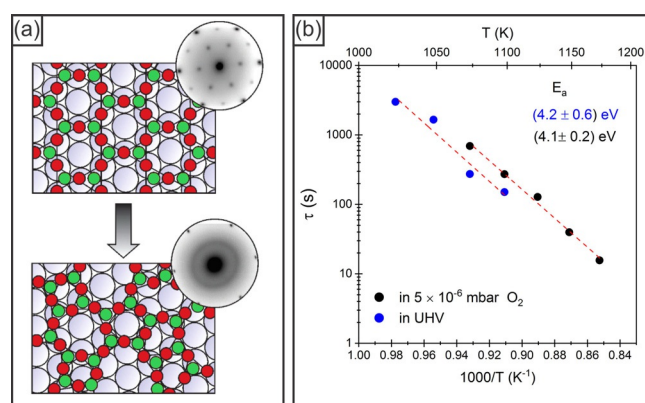


**Figure 8.** Real time studies of the crystalline to vitreous conversion rate of a SiO<sub>2</sub> bilayer film supported on Ru(0001). (a) Atomic models of the crystalline (top) and vitreous (bottom) phases of the silica bilayer film, with their corresponding LEED patterns. Si and O atoms are represented with green and red spheres, respectively. (b) Arrhenius plot of the time constants extracted from the fitting measured at different temperatures in UHV and in O<sub>2</sub> atmosphere for the crystalline to vitreous transition of the metal-supported SiO<sub>2</sub> film. Both figures are reproduced with permission from ref. [125].

Figure 8b shows the Arrhenius analysis of the initial conversion rates of the central (00) LEED spot for the transformation experiments performed in ultrahigh vacuum and in oxygen background pressure. Linear regression of the experimental points yields similar apparent activation energies (4.1 vs. 4.2 eV) for the different atmospheres, with clear differences only in the pre-exponential factor (entropic term) of the Arrhenius expression. DFT calculations performed by M. Sierka and his group<sup>[125]</sup> show that the experimentally obtained energy barriers are consistent with the formation of a Stone–Wales-like defect, resulting in the transformation of four 6-membered rings into two 5- and two 7-membered rings (see above). Interestingly enough, the Ru(0001) support seems to play an important role in the process by stabilizing the local charges generated during the bond rearrangement in the intermediate and transition states of the complex mechanism. Even though the exposed above is the result of integral and averaging measurements, it constitutes the groundwork and determines the direction of future studies with our new instrument capable of unveiling dynamic processes in the atomic scale.<sup>[126]</sup> Finally, we would like to point out that we have not yet observed any recrystallization of the film upon cooling, neither in UHV nor in oxygen atmosphere with cooling rate from 1 to 10 K s<sup>−1</sup>.

### Silica Versus Germania Amorphous Bilayer Films

Figure 9 shows a side-by-side comparison between two STM images of silica and germania amorphous bilayer films supported on Ru(0001) and on Pt(111), respectively. Both STM images are atomically resolved, however, their contrasts correspond to different chemical elements.

The protrusions in the silica bilayer film image (Figure 9, left-hand column) correspond to Si atoms, whereas those in the germania bilayer film (Figure 9, right-hand column) indicate O atomic positions. In Figures 9c and d the protrusions are su-



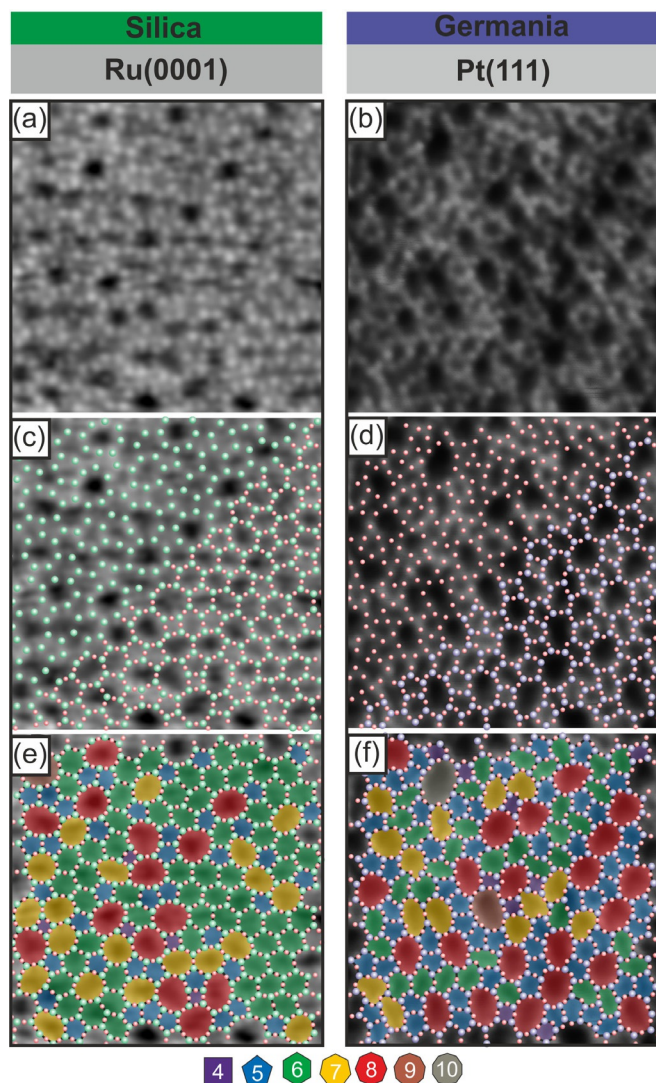


**Figure 9.** STM images of silica (left-hand column) and germania (right-hand column) amorphous bilayer films supported on Ru(0001) and Pt(111), respectively. In Figures (c) and (d), O atoms (red spheres), Ge atoms (blue spheres) and Si atoms (green spheres) are superimposed on the STM images. In Figures (e) and (f), the rings are color-coded according to the code shown at the bottom of the Figure. (a,c,e) 6.6 nm×6.6 nm,  $I_T=0.05$  nA,  $V_S=2.0$  V, adapted from the supplemental material of ref. [3]. (b,d,f) 6.6 nm×6.6 nm,  $I_T=0.1$  nA,  $V_S=0.2$  V, adapted with permission from ref. [19].

perimposed with green and red spheres, respectively. In addition, in the bottom right-hand half of the images the top-most atomic layer is completed by adding the missing anions or cations accordingly. This is achieved, for the silica bilayer film, by adding the O atoms in the intermediate position between two adjacent Si atoms. This procedure is supported by previous studies on silica bilayer films, where Si and O atomic contrast has been simultaneously observed by using a dual mode AFM/STM setup.<sup>[5]</sup> For the germania system, Ge atoms (blue spheres) are placed in the center of the triangles which are formed by the oxygen atoms. Here it is assumed that cations are located in the center of the  $XO_4$  tetrahedra building blocks, whose projection in 2D leads to triangles of three O atoms surrounding the cation. Finally, in Figures 9e and f the top-most layers are

completed and the rings are color-coded according to their sizes. The smallest ring is the 4-membered ring for both systems, and the largest one is for germania the 10-membered ring and for silica the 9-membered ring. However, we have also observed a small amount of 10-membered rings in a different silica preparation on Ru(0001).<sup>[19]</sup>

In the equally-sized STM images in Figures 9a and b, about the same number of rings have been quantified for silica (145) and germania (143), although the Ge–O bonds are longer than the Si–O ones. The similar silica and germania ring density has also been observed in DFT calculated free-standing bilayer films.<sup>[91]</sup> The germania bilayer film is more distorted than the silica one. Whereas the atoms involved in the Si–O–Si bonds are aligned (Figure 9e), the Ge–O–Ge bonds are often bent as viewed from the top (Figure 9f). Additionally, the shape of the silica and germania rings show a different degree of distortion. While the rings of the silica bilayer film tend to form regular polygons; the germania bilayer network presents many strongly distorted rings, typically elongated polygons.

The ring-size distributions for both systems in Figure 9 are illustrated in Figures 10a and b. The silica ring-size distribution shown in Figure 10a is qualitatively equivalent to previous studies that quantified a larger number of rings.<sup>[127]</sup> The main differences between the ring-size statistics of the amorphous germania bilayer film supported on Pt(111) and the amorphous silica bilayer film supported on Ru(0001) are: (1) the most frequent ring in germania is the 5-membered ring, whereas in silica it is the 6-membered ring; (2) the ratio between the 5- and the 6-membered rings is exchanged; (3) germania has a

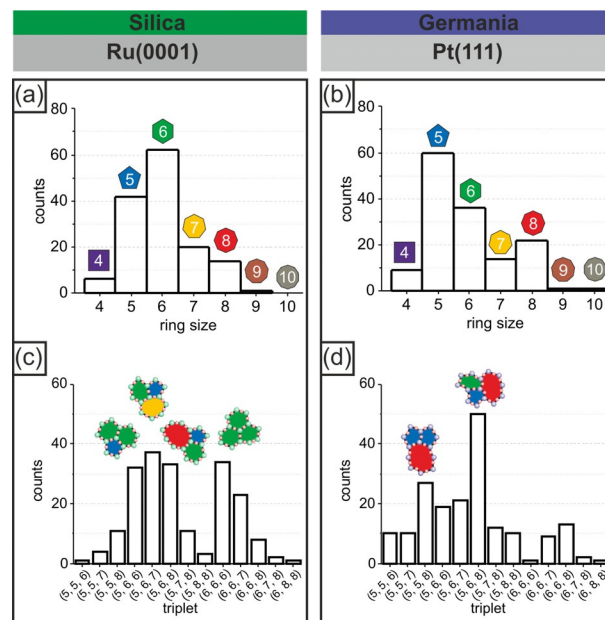


**Figure 10.** Ring-size distribution (upper row) and triplet combination analysis (bottom row) for silica (left-hand column) and germania (right-hand column) amorphous bilayer films supported on Ru(0001) and Pt(111), respectively. The analysis is performed for both networks shown in the STM images in Figure 9. The most frequent triplet combinations are drawn above the corresponding peaks, bottom row. (b) and (d) are taken with permission from ref. [19].

larger number of 8-membered rings and less 7-membered rings. In both cases the amount of 4-, 9- and 10-membered rings remains low. The Euler theorem applied to 2D systems establishes the balance that must exist between the number of rings smaller and larger than 6-membered rings, to maintain a flat system:<sup>[128]</sup> [Eq. (2)]

$$\sum n_x(x-6) = 0 \quad (2)$$

Where  $n_x$  is the number of  $x$ -membered rings. The summation in the left-hand side of Eq. (2) taken over the ring statistics (Figures 10a and b) of the silica and the germania bilayer films give a result of 3 and 13, respectively. Since both systems are atomically flat, as judged with the STM, and they are formed exclusively of polygons of 4 to 10 sides, we would expect that the summation results „zero“ for both systems. However, there are two additional aspects to consider. The first one, the sample space is finite and the edge effect may result in not exactly zero after summation. Second, the equation assumes only the presence of regular polygons. Since the germania bilayer film exhibits mostly irregular-shaped rings, the Euler equation is no longer valid and gives a result far from zero, even though the film is atomically flat. Conversely, in the silica bilayer film, which is constituted by mostly regular rings, the summation in Eq. (2) gives as a result 3, which is close to fulfilling the equation.<sup>[129]</sup> This subtle discrepancy is explained partially by the edge effect and by the non-perfectly regular polygons that constitute the film.

In Figures 10c and d, the triplet combination occurrence in the silica bilayer phase with respect to the germania one, are compared. For clarity, triplets that include 4-, 9- and 10-membered rings are scarce and are not included in the Figure. A more complete triplet combination analysis for the silica bilayer film supported on Ru(0001) can be found in the literature [130], however, both investigations provide qualitatively similar results. When comparing both histograms, one evidences a correlation between the most frequent triplet combinations and the rings involved in the most stable crystalline structures in silica and germania bilayer films. In the case of germania, the 558 unit cell of the germania crystalline bilayer film is manifested in the high occurrence of the (5,5,8) triplet combination (Figure 10d). Additionally, the most frequent triplet combination, the (5,6,8), is present in the linear chains of 6-membered rings that are introduced as defect structures in germania crystalline bilayer films.<sup>[19]</sup> This defect also introduces (6,6,8) and (5,6,6) triplets, which are also frequent in the amorphous phase.

On the other hand, all triplet combinations in the amorphous silica bilayer film (Figure 10c) contain 6-membered rings, including the (6,6,6) triplet, in line with the preferred crystalline hexagonal phase in silica bilayer films on Ru(0001). Silica films also show a correlation between the most frequent triplets and the ring-combinations which form defect structures in the crystalline phase. For instance, the most common defect in crystalline silica bilayer films supported on Ru(0001) is the 558 antiphase boundary structure.<sup>[112]</sup> One unit cell of this defect contains ten triplet combinations, four of them are

(5,6,8) triplets, and the (5,6,6), (5,5,8) and (6,6,8) are repeated twice each. One can see in Figure 10c that all these four different triplet combinations are preferred ones. In Table 3 we see that the silica crystalline bilayer film supported on Ru(0001) forms also other defect structures that involve 5- and 7-membered rings, and a 48 domain boundary. The former ones introduce triplets such as (5,6,7) and (6,6,7), both of them preferred triplet combinations in the amorphous phase. The 48 domain boundary is not evidenced in any preferred ring combination in the amorphous phase due to the small number of 4-membered rings in the film. K. Burson et al. investigated in detail the correlation between the different rings that form defects in the silica crystalline bilayer film grown on Ru(0001) and in its amorphous phase.<sup>[112]</sup> Similarities in the ring combinations and statistics were found, however a clear difference lies in their order and periodicity. In bulk materials, crystalline regions of cristobalite are observed in vitreous silica and germania which increase in size upon devitrification.<sup>[32]</sup>

There is a significantly small number of the (6,6,6) triplets in the germania amorphous bilayer film supported on Pt(111), despite the fact that the 6-membered rings are the second most frequent ring-size (Figure 10, right column). This observation is in agreement with the impact of the crystalline unit cell of the support on the amorphous ring-size distribution, discussed above. Moreover, DFT calculations of free-standing germania and silica bilayer films predict the hexagonal phase to be the most stable one in both systems.<sup>[91, 19]</sup> Consequently, the 558 crystalline phase observed in germania bilayer films and the lack of (6,6,6) triplet combinations is attributed to the influence of the metal-support on the film structure.<sup>[19]</sup>

## Conclusions and Outlook

Ultrathin films of silica and germania have been prepared on different substrates and characterized at the atomic scale using a combination of surface science techniques, specifically high-resolution scanning probe microscopy, LEED, and I/V-LEED, as well as theoretical modeling with DFT calculations.

Monolayer films of silica grown on Mo(112) consist of a two-dimensional network of corner sharing SiO<sub>4</sub> tetrahedra, with one oxygen of each tetrahedron binding to the protruding Mo atoms of the Mo(112) surface.<sup>[54, 55]</sup> On Ru(0001) a monolayer with a similar structure to that found on Mo(112) is formed, which also shows a (2×2) periodicity in the LEED pattern and where the IRAS spectrum indicates the presence of Si-O-Ru bonds.<sup>[66, 68, 69]</sup>

At low coverages, the STM images of ultrathin films of germania on Ru(0001) revealed a hexagonal structure of O and Ge atoms, whereas the LEED pattern exhibited a (2×2) periodicity with respect to the metal-support. Subsequently, an I/V-LEED study determined that the film consists of a network of GeO<sub>4</sub> building blocks forming a strongly coupled monolayer film of 6-membered rings. Furthermore, different ring-sizes were observed in diverse boundary structures. At higher coverage, an amorphous bilayer film is observed. However, its strong interaction with the metal-support, as determined by DFT calculations, causes an ill-defined and corrugated film. In short, on

Ru(0001), stable hexagonal monolayer films are formed, characterised by strong Ge–O–Ru-bonds which avoid the formation of atomically flat decoupled bilayer films.

For ultrathin films of germania supported on Pt(111), the largest number of polymorphs have been observed: two types of monolayer films, a zigzag phase, and bilayer films with different degree of order. The monolayer films undergo a significant distortion in order to adapt to the support. In one case, three different sized 6-membered rings arranged in a (3×3) superstructure and, in another case a combination of 8-, 6- and 4-membered rings forming a rectangular unit cell. In the latter film, the distortion is such that the DFT model predicts the presence of 5-coordinated Ge atoms.<sup>[19,93]</sup>

Well-defined bilayer films were prepared and characterized in detail. By varying the temperature, the structural changes from crystalline to mixed crystalline and amorphous to purely amorphous phases can be tuned in a controlled manner. Whereas the crystalline phase presents an oblique unit cell formed by 8- and 5-membered rings, the amorphous phase exhibits a ring-size distribution that ranges from 4- to 10-membered rings. The latter film constitutes a new well-defined 2D amorphous model system with similarities and differences to the corresponding Si-based material. The germania bilayer film, like the silica one, is formed by a double layer of GeO<sub>4</sub> building blocks which are chemically decoupled from the metal support. However, in comparison to the silica bilayer film, the germania film shows a larger corrugation. Moreover, the ring-size distributions of its crystalline and amorphous phase are influenced by the interaction with the Pt(111) metal-support.

The investigation of germania films supported on an oxygen inert Au(111) surface leads to a clear picture of the role of the substrate on the resulting film structure. The Au(111) surface shows a herringbone reconstruction which acts as a sensor for the strength of the film–substrate interaction. The decoupling of the film from the Au(111) support has been evidenced by the behavior of the native configuration of the fcc and hcp stacking of the reconstructed Au(111) top layer atoms.<sup>[121]</sup> The reconstruction persists underneath the germania bilayer patches. This observation differs from the general behavior of oxide films which lift the Au(111) reconstruction. Consequently, these films form only amorphous bilayers, as expected from the trend observed in silica films supported on different metal supports. DFT calculations also predicted a very weak film–substrate interaction for the germania on Au(111) system (see Table 4). Moreover, the presence of the (6,6,6) triplet combination, as a preferred one, suggested that the film is little influenced by the metal–support and its structure may resemble more the calculated one for free-standing germania bilayer films.

On identical metal–substrates (Ru(0001) and Pt(111)), the films of germania interact stronger with the support than the silica films (see Table 4). This finding points to an interesting parallelism between metal-supported germania and silica films. Specifically, the silica network structures supported on Mo(112), Ru(0001) and Pt(111) correspond closely to those of germania on Ru(0001), Pt(111), and Au(111), respectively. This behaviour underscores the important role of the film–substrate

interaction, reflected in the calculated adhesion energies. In systems where the adhesion energies are very weak, e.g., for germania on Au(111) an amorphous film growth is promoted.

Another obvious interesting future development is to prepare mixed silica-germania films trying to achieve a complete mixing at the atomic level. A. B. Fuhrich,<sup>[131]</sup> in his dissertation, has undertaken the first attempts to prepare such films, controlling the preparation conditions using LEEM, XPS and I/V-LEED information. The ensemble averaging studies indicate, that it is possible to achieve intimately mixed crystalline silica-germania layers. Future studies need to show how those are structured at the atomic level with respect to Si and Ge distributions.

To conclude, the orientation of adjacent rings, the ring-size distribution, and the ring-triplets analysis for each silica and germania film phase formed on the metal supports Mo(112), Ru(0001), Pt(111), and Au(111), together with DFT calculations, clearly suggest that the atomic network structure of silica and germania ultrathin films is strongly influenced by the film–support interaction. Our experiments and the theoretical modeling highlight quantitatively the impact of the metal–support on the oxide film structure concerning strain, adhesion energy, charge transfer, work function, and, most importantly in the present context of glass-forming materials, the pathway of crystalline towards amorphous film growth. This work provides a useful generalization of the relationship between adhesion energy and film structure. Possible applications abound: Amorphous networks, 2D-materials, zeolites and more.

## Experimental and Computational Methods

The metal-supported films are prepared and characterized in ultra-high vacuum conditions (UHV) (base pressure 10<sup>−10</sup> mbar range). The Ru(0001), Pt(111) and Au(111) single-crystals are cleaned following the procedures reviewed by R. G. Musket et al.<sup>[132]</sup> Si(Ge) is evaporated by physical vapor deposition (PVD) and subsequently annealed in O<sub>2</sub> to produce well-defined silica(germania) films. The specific preparation conditions for each silica and germania film system are reported in refs. [54, 2, 21, 66, 22, 67] and refs. [17, 19, 20], respectively. The LEEM/LEED experiments were carried out in the SMART microscope operating at the UE49-PGM beam line of the synchrotron light source BESSY II of the Helmholtz Centre Berlin (HZB).

DFT calculations are performed on periodic slab models with the code VASP, relying on the PBE functional corrected for long-range dispersion according to the D2' Scheme. A full description of the methodology is enclosed in refs. [18–20].

## Acknowledgements

This project has received funding from the European Research Council (ERC) under the European Union's Horizon 2020 Research and Innovation Program (Grant Agreement No. 669179). We thank the BESSY II crew for their support and the Helmholtz-Center Berlin for Materials and Energy (HZB) for the allocation of beamtime. M.P., A.F. and T.S. acknowledge the financial support by the Federal German Ministry of Education and



Science (BMBF) under Contract No. 05KS4WWB/4. S.T. and G.P. thank the Italian MIUR for financial support through the PRIN 2017 Project MULTI-e and CINECA for granting access to super-computing resources via the ISCRA initiative. Open access funding enabled and organized by Projekt DEAL.

## Conflict of interest

The authors declare no conflict of interest.

**Keywords:** amorphous structures · crystalline materials · germania · metal-supported films · silica

- [1] A. C. Wright, M. F. Thorpe, *Phys. Status Solidi B* **2013**, *250*, 931–936.
- [2] D. Löffler, J. J. Uhlrich, M. Baron, B. Yang, X. Yu, L. Lichtenstein, L. Heinke, C. Büchner, M. Heyde, S. Shaikhutdinov, H.-J. Freund, R. Włodarczyk, M. Sierka, J. Sauer, *Phys. Rev. Lett.* **2010**, *105*, 146104.
- [3] L. Lichtenstein, M. Heyde, H.-J. Freund, *Phys. Rev. Lett.* **2012**, *109*, 106101.
- [4] W. H. Zachariasen, *J. Am. Chem. Soc.* **1932**, *54*, 3841–3851.
- [5] L. Lichtenstein, M. Heyde, H.-J. Freund, *J. Phys. Chem. C* **2012**, *116*, 20426–20432.
- [6] C. Büchner, Z.-J. Wang, K. M. Burson, M.-G. Willinger, M. Heyde, R. Schlögl, H.-J. Freund, *ACS Nano* **2016**, *10*, 7982–7989.
- [7] H.-J. Freund, M. Heyde, C. Büchner, U.S. patent number 10,763,102 [Application Number 16/083,338] was granted by the patent office on 2020-09-01 for “transferable silica bilayer film”.
- [8] S. Ulrich, N. Nilius, H.-J. Freund, U. Martinez, L. Giordano, G. Pacchioni, *Surf. Sci.* **2009**, *603*, 1145–1149.
- [9] C. Büchner, L. Lichtenstein, S. Stucklenholz, M. Heyde, F. Ringleb, M. Sterrer, W. E. Kaden, L. Giordano, G. Pacchioni, H.-J. Freund, *J. Phys. Chem. C* **2014**, *118*, 20959–20969.
- [10] W. E. Kaden, C. Büchner, L. Lichtenstein, S. Stucklenholz, F. Ringleb, M. Heyde, M. Sterrer, H.-J. Freund, L. Giordano, G. Pacchioni, C. J. Nelin, P. S. Bagus, *Phys. Rev. B* **2014**, *89*, 115436.
- [11] J.-Q. Zhong, M. Wang, N. Akter, J. D. Kestell, A. M. Boscoboinik, T. Kim, D. J. Stacchiola, D. Lu, J. Anibal Boscoboini, *Nat. Commun.* **2017**, *8*, 16118.
- [12] M. J. Prieto, H. W. Klemm, F. Xiong, D. M. Gottlob, D. Menzel, T. Schmidt, H.-J. Freund, *Angew. Chem. Int. Ed.* **2018**, *57*, 8749–8753; *Angew. Chem.* **2018**, *130*, 8885–8889.
- [13] G. Barcaro, A. Fortunelli, *Phys. Chem. Chem. Phys.* **2019**, *21*, 11510–11536.
- [14] R. Mas-Ballesté, C. Gómez-Navarro, J. Gómez-Herrero, F. Zamora, *Nanoscale* **2011**, *3*, 20–30.
- [15] A. Gupta, T. Sakthivel, S. Seal, *Prog. Mater. Sci.* **2015**, *73*, 44–126.
- [16] X. Yu, B. Yang, J. Anibal Boscoboinik, S. Shaikhutdinov, H.-J. Freund, *Appl. Phys. Lett.* **2012**, *100*, 151608.
- [17] A. L. Lewandowski, P. Schlexer, C. Büchner, E. M. Davis, H. Burrall, K. M. Burson, W.-D. Schneider, M. Heyde, G. Pacchioni, H.-J. Freund, *Phys. Rev. B* **2018**, *97*, 115406.
- [18] A. L. Lewandowski, P. Schlexer, S. Tosoni, L. Gura, P. Marschalik, C. Büchner, H. Burrall, K. M. Burson, W.-D. Schneider, G. Pacchioni, M. Heyde, *J. Phys. Chem. C* **2019**, *123*, 7889–7897.
- [19] A. L. Lewandowski, S. Tosoni, L. Gura, P. Schlexer, P. Marschalik, W.-D. Schneider, M. Heyde, G. Pacchioni, H.-J. Freund, *Angew. Chem. Int. Ed.* **2019**, *58*, 10903–10908; *Angew. Chem.* **2019**, *131*, 11019–11024.
- [20] A. L. Lewandowski, F. Stavale, S. Tosoni, W.-D. Schneider, M. Heyde, G. Pacchioni, H.-J. Freund, *Phys. Rev. B* **2019**, *100*, 241403.
- [21] L. Lichtenstein, C. Büchner, B. Yang, S. Shaikhutdinov, M. Heyde, M. Sierka, R. Włodarczyk, J. Sauer, H.-J. Freund, *Angew. Chem. Int. Ed.* **2012**, *51*, 404–407; *Angew. Chem.* **2012**, *124*, 416–420.
- [22] D. Kuhness, H. J. Yang, H. W. Klemm, M. Prieto, G. Peschel, A. Fuhrich, D. Menzel, T. Schmidt, X. Yu, S. Shaikhutdinov, A. Lewandowski, M. Heyde, A. Kelemen, R. Włodarczyk, D. Usyat, M. Schütz, J. Sauer, H.-J. Freund, *J. Am. Chem. Soc.* **2018**, *140*, 6164–6168.
- [23] M. Micoulaut, L. Cormier, G. S. Henderson, *J. Phys. Condens. Matter* **2006**, *18*, R753.
- [24] L. Pauling, *The Nature of the Chemical Bond*, Vol. 260, Cornell University Press, Ithaca, **1960**.
- [25] G. S. Smith, P. B. Isaacs, *Acta Crystallogr.* **1964**, *17*, 842–846.
- [26] J. Haines, O. Cambon, E. Philippot, L. Chapon, S. Hull, *J. Solid State Chem.* **2002**, *166*, 434.
- [27] J. D. Jorgensen, *J. Appl. Phys.* **1978**, *49*, 5473–5478.
- [28] A. A. Lebedev, *Trudy Gosudarstvennogo Opticheskogo Instituta Proceedings of the State Optical Institute* **1921**, *2*, 1–20.
- [29] B. E. Warren, *Phys. Rev.* **1934**, *45*, 657.
- [30] B. E. Warren, *J. Am. Ceram. Soc.* **1934**, *17*, 249–254.
- [31] A. J. Leadbetter, A. C. Wright, *J. Non-Crystalline Solids* **1972**, *7*, 37–52.
- [32] A. C. Wright, *Phys. Chem. Glasses—Eur. J. Glass Sci. Technol. B* **2019**, *60*, 33–48.
- [33] J. D. Mackenzie, *Modern Aspects of the Vitreous State*, Vol. 2, Butterworths, Oxford, **1960**.
- [34] A. C. Wright, *Int. J. Appl. Glass Sci.* **2014**, *5*, 31–56.
- [35] D. L. Price, M.-L. Saboungi, A. C. Barnes, *Phys. Rev. Lett.* **1998**, *81*, 3207.
- [36] A. C. Wright, *J. Non-Cryst. Solids* **1994**, *179*, 84–115.
- [37] R. L. Mozzi, B. E. Warren, *J. Appl. Crystallogr.* **1969**, *2*, 164–172.
- [38] J. A. E. Desa, A. C. Wright, R. N. Sinclair, *J. Non-Cryst. Solids* **1988**, *99*, 276–288.
- [39] P. Richet, *Phys. Chem. Min.* **1990**, *17*, 79–88.
- [40] J. Neufeind, K. D. Liss, *Ber. Bunsenges. Phys. Chem.* **1996**, *100*, 1341–1349.
- [41] F. Mauri, A. Pasquarello, B. G. Pfrommer, Y.-G. Yoon, S. G. Louie, *Phys. Rev. B* **2000**, *62*, R4786.
- [42] P. S. Salmon, A. C. Barnes, R. A. Martin, G. J. Cuello, *J. Phys. Condens. Matter* **2007**, *19*, 415110.
- [43] F. L. Galeener, *Solid State Commun.* **1982**, *44*, 1037.
- [44] R. A. Barrio, F. L. Galeener, E. Martínez, R. J. Elliott, *Phys. Rev. B* **1993**, *48*, 15672.
- [45] C. R. Helms, E. H. Poindexter, *Rep. Progr. Phys.* **1994**, *57*, 791.
- [46] Z. Wang, H. Wang, A. Mitra, L. Huang, Y. Yan, *Adv. Mater.* **2001**, *13*, 746–749.
- [47] E. L. Margelefsky, R. K. Zeidan, M. E. Davis, *Chem. Soc. Rev.* **2008**, *37*, 1118–1126.
- [48] J. Yao, L. Zhong, D. Natelson, J. M. Tour, *J. Am. Chem. Soc.* **2011**, *133*, 941–948.
- [49] S. Minakata, M. Komatsu, *Chem. Rev.* **2009**, *109*, 711–724.
- [50] E. Groppo, C. Lamberti, S. Bordiga, G. Spoto, A. Zecchina, *Chem. Rev.* **2005**, *105*, 115–184.
- [51] T. Schroeder, M. Adelt, B. Richter, M. Naschitzki, M. Bäumer, H.-J. Freund, *Surf. Rev. Lett.* **2000**, *7*, 7–14.
- [52] T. Schroeder, J. B. Giorgi, M. Bäumer, H.-J. Freund, *Phys. Rev. B* **2002**, *66*, 165422.
- [53] M. S. Chen, A. K. Santra, D. W. Goodman, *Phys. Rev. B* **2004**, *69*, 155404.
- [54] J. Weissenrieder, S. Kaya, J.-L. Lu, H.-J. Gao, S. Shaikhutdinov, H.-J. Freund, M. Sierka, T. K. Todorova, J. Sauer, *Phys. Rev. Lett.* **2005**, *95*, 076103.
- [55] L. Giordano, D. Ricci, G. Pacchioni, P. Uglieng, *Surf. Sci.* **2005**, *584*, 225–236.
- [56] S. Ulrich, N. Nilius, H.-J. Freund, *Phys. Rev. Lett.* **2009**, *102*, 016102.
- [57] B. Yang, E. Emmez, W. E. Kaden, X. Yu, J. A. Boscoboinik, M. Sterrer, S. Shaikhutdinov, H.-J. Freund, *J. Phys. Chem. C* **2013**, *117*, 8336–8344.
- [58] E. Emmez, B. Yang, S. Shaikhutdinov, H.-J. Freund, *J. Phys. Chem. C* **2014**, *118*, 29034–29042.
- [59] J. A. Boscoboinik, *J. Phys. Condens. Matter* **2018**, *31*, 063001.
- [60] N. Akter, M. Wang, J.-Q. Zhong, Z. Liu, T. Kim, D. Lu, J. Anibal Boscoboinik, D. J. Stacchiola, *Top. Catal.* **2018**, *61*, 419–427.
- [61] M. Wang, Ch. Zhou, N. Akter, W. T. Tysoe, J. A. Boscoboinik, D. Lu, *ACS Catal.* **2020**, *10*, 6119–6128.
- [62] D. Stacchiola, S. Kaya, J. Weissenrieder, H. Kühlenbeck, S. Shaikhutdinov, H.-J. Freund, M. Sierka, T. Kumanova Todorova, J. Sauer, *Angew. Chem. Int. Ed.* **2006**, *45*, 7636–7639; *Angew. Chem.* **2006**, *118*, 7798–7801.
- [63] J. W. He, X. Xu, J. S. Corneille, D. W. Goodman, *Surf. Sci.* **1992**, *279*, 119–126.
- [64] X. Xu, D. W. Goodman, *Appl. Phys. Lett.* **1992**, *61*, 774–776.

- [65] D. J. Stacchiola, M. Baron, S. Kaya, J. Weissenrieder, S. Shaikhutdinov, H.-J. Freund, *Appl. Phys. Lett.* **2008**, *92*, 011911.
- [66] B. Yang, W. E. Kaden, X. Yu, J. A. Boscoboinik, Y. Martynova, L. Lichtenstein, M. Heyde, M. Sterrer, R. Włodarczyk, M. Sierka, J. Sauer, S. Shaikhutdinov, H.-J. Freund, *Phys. Chem. Chem. Phys.* **2012**, *14*, 11344–11351.
- [67] H. W. Klemm, M. J. Prieto, G. Peschel, A. Fuhrich, E. Madej, F. Xiong, D. Menzel, T. Schmidt, H.-J. Freund, *J. Phys. Chem. C* **2019**, *123*, 8228–8243.
- [68] B. Yang, J. A. Boscoboinik, X. Yu, S. Shaikhutdinov, H.-J. Freund, *Nano Lett.* **2013**, *13*, 4422–4427.
- [69] S. Mathur, S. Vlaic, E. Machado-Charry, A.-D. Vu, V. Guisset, P. David, E. Hadji, P. Pochet, J. Coraux, *Phys. Rev. B* **2015**, *92*, 161410.
- [70] X. Yuan, A. N. Cormack, *J. Non-Crystall. Solids* **2001**, *283*, 69–87.
- [71] A. Tilocca, N. H. de Leeuw, A. N. Cormack, *Phys. Rev. B* **2006**, *73*, 104209.
- [72] A. Pedone, G. Malavasi, M. C. Menziani, A. N. Cormack, U. Segre, *J. Phys. Chem. B* **2006**, *110*, 11780–11795.
- [73] A. Pedone, *J. Phys. Chem. C* **2009**, *113*, 20773–20784.
- [74] S. Urata, H. Yoshino, M. Ono, S. Miyasaka, R. Ando, Y. Hayashi, *J. Phys. Chem. C* **2018**, *122*, 28204–28214.
- [75] M. Wilson, A. Kumar, D. Sherrington, M. F. Thorpe, *Phys. Rev. B* **2013**, *87*, 214108.
- [76] C. Büchner, *Adding a Novel Material to the 2D Toolbox: Properties and Transfer of a Silica Bilayer*, PhD thesis, Humboldt Universität zu Berlin, **2016**.
- [77] L. Lichtenstein, M. Heyde, S. Ulrich, N. Nilius, H.-J. Freund, *J. Phys. Condens. Matter* **2012**, *24*, 354010.
- [78] E. Gao, B. Xie, Z. Xu, *J. Appl. Phys.* **2016**, *119*, 014301.
- [79] E. Emmez, J. A. Boscoboinik, S. Tenney, P. Sutter, S. Shaikhutdinov, H.-J. Freund, *Surf. Sci.* **2016**, *646*, 19–25.
- [80] H. Tissot, X. Wenig, P. Schlexer, G. Pacchioni, S. Shaikhutdinov, H.-J. Freund, *Surf. Sci.* **2018**, *678*, 118–123.
- [81] C. Büchner, S. D. Eder, T. Nesse, D. Kuhness, P. Schlexer, G. Pacchioni, J. R. Manson, M. Heyde, B. Holst, H.-J. Freund, *Phys. Rev. Lett.* **2018**, *120*, 226101.
- [82] J. A. Boscoboinik, X. Yu, B. Yang, F. D. Fischer, R. Włodarczyk, M. Sierka, S. Shaikhutdinov, J. Sauer, H.-J. Freund, *Angew. Chem. Int. Ed.* **2012**, *51*, 6005–6008; *Angew. Chem.* **2012**, *124*, 6107–6111.
- [83] J. A. Boscoboinik, X. Yu, B. Yang, S. Shaikhutdinov, H.-J. Freund, *Microp. Mesop. Mater.* **2013**, *165*, 158–162.
- [84] C. Zhou, X. Liang, G. S. Hutchings, Z. S. Fishman, J.-H. Jhang, M. Li, U. D. Schwarz, S. Ismail-Beigi, E. I. Altman, *Chem. Mater.* **2019**, *31*, 851–861.
- [85] K. M. Burson, L. Gura, B. Kell, C. Büchner, A. L. Lewandowski, M. Heyde, H.-J. Freund, *Appl. Phys. Lett.* **2016**, *108*, 201602.
- [86] P. Y. Huang, S. Kurasch, A. Srivastava, V. Skakalova, J. Kotakoski, A. V. Krasheninnikov, R. Hovden, Q. Mao, J. C. Meyer, J. Smet, D. A. Müller, U. Kaiser, *Nano Lett.* **2012**, *12*, 1081–1086.
- [87] J.-H. Jhang, C. Zhou, O. E. Dagdeviren, G. S. Hutchings, U. D. Schwarz, E. I. Altman, *Phys. Chem. Chem. Phys.* **2017**, *19*, 14001–14011.
- [88] E. I. Altman, J. Götzen, N. Samudrala, U. D. Schwarz, *J. Phys. Chem. C* **2013**, *117*, 26144–26155.
- [89] E. I. Altman, U. D. Schwarz, *Adv. Mater. Interfaces* **2014**, *1*, 1400108.
- [90] G. S. Hutchings, J.-H. Jhang, C. Zhou, D. Hynek, U. D. Schwarz, E. I. Altman, *ACS Appl. Mater. Interfaces* **2017**, *9*, 11266–11271.
- [91] A. Malashevich, S. Ismail-Beigi, E. I. Altman, *J. Phys. Chem. C* **2016**, *120*, 26770–26781.
- [92] C. N. R. Rao, P. V. Kamath, S. Yashonath, *Chem. Phys. Lett.* **1982**, *88*, 13–16.
- [93] A. L. Lewandowski, *The Atomic Structure of Ultrathin Germania Films*, PhD thesis, Humboldt Universität, **2019**.
- [94] B. A. Staskiewicz, J. R. Tucker, P. E. Snyder, *J. Am. Chem. Soc.* **1955**, *77*, 2987–2989.
- [95] R. J. D. Tilley, *Principles and Applications of Chemical Defects*, CRC Press, Boca Raton, **1998**.
- [96] H. Xiao, I. Baker, *Acta Metall. Mater.* **1995**, *43*, 391–396.
- [97] M. Sammalkorpi, A. V. Krasheninnikov, A. Kuronen, K. Nordlund, K. Kaski, *Phys. Rev. B* **2004**, *70*, 245416.
- [98] R. Grantab, V. B. Shenoy, R. S. Ruoff, *Science* **2010**, *330*, 946.
- [99] D. L. Griscom, *J. Ceramic Soc. Japan* **1991**, *99*, 923–942.
- [100] D. B. Holt, B. G. Yacobi, *Extended Defects in Semiconductors: Electronic Properties, Device Effects and Structures*, Cambridge University Press, Cambridge, **2007**.
- [101] M. J. Puska, *J. Phys. Condens. Matter* **1989**, *1*, 7347.
- [102] T. L. Thompson, J. T. Yates, *Chem. Rev.* **2006**, *106*, 4428–4453.
- [103] J. Paier, C. Penschke, J. Sauer, *Chem. Rev.* **2013**, *113*, 3949–3985.
- [104] D. M. Smyth, *The Defect Chemistry of Metal Oxides*, Oxford University Press, Oxford, **2000**.
- [105] G. Pacchioni, *Surf. Rev. Lett.* **2000**, *7*, 277–306.
- [106] O. Bikondoa, C. L. Pang, R. Ithnin, C. A. Muryn, H. Onishi, G. Thornton, *Nat. Mater.* **2006**, *5*, 189.
- [107] C. T. Campbell, C. H. F. Peden, *Science* **2005**, *309*, 713–714.
- [108] J. Jupille, G. Thornton, *Defects at Oxide Surfaces, Vol. 58*, Springer, Heidelberg, **2015**.
- [109] J. C. Meyer, C. Kisielowski, R. Erni, M. D. Rossell, M. F. Crommie, A. Zettl, *Nano Lett.* **2008**, *8*, 3582–3586.
- [110] J. Kotakoski, A. V. Krasheninnikov, U. Kaiser, J. C. Meyer, *Phys. Rev. Lett.* **2011**, *106*, 105505.
- [111] J. Lahiri, M. Batzill, *Nat. Nanotechnol.* **2010**, *5*, 326.
- [112] K. M. Burson, C. Büchner, M. Heyde, H.-J. Freund, *J. Phys. Condens. Matter* **2017**, *29*, 035002.
- [113] D. L. Duong, G. H. Han, S. M. Lee, F. Gunes, E. S. Kim, S. T. Kim, H. Kim, Q. H. Ta, K. P. So, S. J. Yoon, S. J. Chae, Y. W. Jo, M. H. Park, S. H. Chae, S. C. Lim, J. Y. Choi, Y. H. Lee, *Nature* **2012**, *490*, 235.
- [114] P. Y. Huang, C. S. Ruiz-Vargas, A. M. van der Zande, W. S. Whitney, S. Garg, J. S. Alden, C. J. Hustedt, Y. Zhu, J. Park, P. L. McEuen, D. A. Muller, *Nature* **2011**, *469*, 389.
- [115] Y. Wei, J. Wu, H. Yin, X. Shi, R. Yang, M. Dresselhaus, *Nat. Mater.* **2012**, *11*, 759.
- [116] F. Banhart, J. Kotakoski, A. V. Krasheninnikov, *ACS Nano* **2011**, *5*, 26–41.
- [117] M. T. Lusk, L. D. Carr, *Phys. Rev. Lett.* **2008**, *100*, 175503.
- [118] M. T. Lusk, D. T. Wu, L. D. Carr, *Phys. Rev. B* **2010**, *81*, 155444.
- [119] A. J. Stone, D. J. Wales, *Chem. Phys. Lett.* **1986**, *128*, 501.
- [120] K. Lauwaet, K. Schouteden, E. Janssens, C. Van Haesendonck, P. Lievens, M. I. Trioni, L. Giordano, G. Pacchioni, *Phys. Rev. B* **2012**, *85*, 245440.
- [121] J. V. Barth, H. Brune, G. Ertl, R. J. Behm, *Phys. Rev. B* **1990**, *42*, 9307.
- [122] H.-Y. T. Chen, G. Pacchioni, *Phys. Chem. Chem. Phys.* **2014**, *16*, 21838–21845.
- [123] F. Rossel, M. Pivetta, F. Patthey, E. Čavar, A. P. Seitsonen, W.-D. Schneider, *Phys. Rev. B* **2011**, *84*, 075426.
- [124] H. Junkes, et al., Proc. of International Conference on Accelerator and Large Experimental Control Systems (ICALPECS'17), Barcelona, Spain, 8–13 October 2017 (Barcelona, Spain). International Conference on Accelerator and Large Experimental Control Systems 16. Geneva, Switzerland: JACoW, Jan. **2018**, pp. 1762–1766.
- [125] H. W. Klemm, M. J. Prieto, F. Xiong, G. B. Hassine, M. Heyde, D. Menzel, M. Sierka, T. Schmidt, H.-J. Freund, *Angew. Chem. Int. Ed.* **2020**, *59*, 10587–10593; *Angew. Chem.* **2020**, *132*, 10674–10680.
- [126] H.-J. Freund, *Acc. Chem. Res.* **2017**, *50*, 446–449.
- [127] L. Lichtenstein, *The Structure of Two-Dimensional Vitreous Silica*, PhD thesis, Freie Universität Berlin, **2012**.
- [128] T. W. Ebbesen, *Acc. Chem. Res.* **1998**, *31*, 558.
- [129] K. M. Burson, P. Schlexer, C. Büchner, L. Lichtenstein, M. Heyde, H.-J. Freund, *J. Chem. Ed.* **2015**, *92*, 1896–1902.
- [130] C. Büchner, L. Liu, S. Stuckenholtz, K. M. Burson, L. Lichtenstein, M. Heyde, H.-J. Gao, H.-J. Freund, *J. Non-Cryst. Solids* **2016**, *435*, 40–47.
- [131] A. B. Fuhrich, *Ultra-thin Germania and Germania-Silica films: Growth, Structure and Reactivity*, PhD thesis, Freie Universität Berlin, **2019**.
- [132] R. G. Musket, W. McLean, C. A. Colmenares, D. M. Makowiecki, W. J. Siekhaus, *Appl. Surf. Sci.* **1982**, *10*, 143.

Manuscript received: April 14, 2020

Revised manuscript received: July 6, 2020

Accepted manuscript online: July 20, 2020

Version of record online: December 9, 2020